

Vertically Sheared Horizontal Flow-Forming Instability in Stratified Turbulence: Linear Stability Analysis using the Analytical Approach to Statistical State Dynamics

JOSEPH G. FITZGERALD* AND BRIAN F. FARRELL

Department of Earth and Planetary Sciences, Harvard University, Cambridge, Massachusetts

ABSTRACT

Vertically banded zonal jets are frequently observed in weakly or non-rotating stratified turbulence, with the quasi-biennial oscillation in the equatorial stratosphere and the ocean's equatorial deep jets being two examples. Explaining the formation of jets in stratified turbulence is a fundamental problem in geophysical fluid dynamics. Statistical state dynamics (SSD) provides powerful methods for analyzing turbulent systems exhibiting emergent organization, such as banded jets. In SSD, dynamical equations are written directly for the evolution of the turbulent statistics, enabling direct analysis of the statistical interactions between incoherent turbulence and coherent large-scale structure that underlie jet formation. A second-order closure of SSD, known as S3T, has previously been applied to show that meridionally banded jets emerge in barotropic β -plane turbulence via a statistical instability sometimes called zonostrophic instability (ZI). Two-dimensional (2D) Boussinesq turbulence provides a simple model of non-rotating stratified turbulence analogous to the β -plane model of planetary turbulence. Jets known as vertically sheared horizontal flows (VSHFs) often emerge in simulations of Boussinesq turbulence, but their dynamics is not yet clearly understood. In this work the S3T analysis of ZI is extended to study VSHF emergence in 2D Boussinesq turbulence using the analytical approach to S3T. VSHFs are shown to form via an instability associated with negative eddy viscosity that is the analog in stratified turbulence of ZI in β -plane turbulence. This instability is shown to be strikingly similar to ZI, suggesting that jet emergence in both geostrophic and non-rotating stratified turbulence may be conceptualized as instances of the same generic phenomenon.

1. Introduction

Coherent zonal jets are a common feature of geostrophic turbulence. The meridionally banded zonal winds of Jupiter (Vasavada and Showman 2005) and the striations of the Earth's midlatitude oceans (Maximenko et al. 2005) provide striking examples. Zonal jets also emerge in laboratory experiments and numerical simulations modeling the planetary turbulence regime (Williams 1978; Huang and Robinson 1998; Read et al. 2007; Galperin and Read 2017). The barotropic β -plane system has come to serve as the paradigmatic example of zonal jet emergence in planetary turbulence due to its attractive simplicity as well as its role in the problem's history (Rhines 1975).

Organization of geostrophic turbulence into zonal jets is sometimes referred to as 'zonation' (Galperin et al. 2006) and the mechanism of zonation is sometimes referred to as 'zonostrophic instability' (ZI) (Srinivasan and Young 2012). ZI is a statistical instability in which weak jets arise

randomly from turbulent fluctuations or initial conditions break the statistical homogeneity of geostrophic turbulence and organize Reynolds stresses that drive the jets. ZI is intrinsically statistical because the turbulent background upon which ZI occurs is stochastically fluctuating. The interactions between the jets and the turbulence fluctuate in time and space so that mutual reinforcement of the jets and the Reynolds stresses occurs in statistical average but not at each instant or location. Because it is statistical, ZI is obscured in individual realizations of the system but becomes manifest when dynamics are formulated for the statistical state of the turbulence, an approach referred to as statistical state dynamics (SSD) (Farrell and Ioannou 2017a).

Organization of turbulence into persistent zonal jets also occurs in weakly- and non-rotating stratified turbulence. Vertically banded (or 'stacked') jets known as equatorial deep jets (EDJs) are observed in all equatorial ocean basins below approximately 1000 m depth and consist of alternating eastward and westward zonal jets with a spacing of approximately 500 m (Youngs and Johnson 2015). The quasi-biennial oscillation (QBO) of the equatorial stratosphere provides another example in which the vertically banded structure takes the form of regularly de-

*Corresponding author address: Joseph G. Fitzgerald, Department of Earth and Planetary Sciences, Harvard University, Geological Museum 404, 24 Oxford Street, Cambridge, MA 02138
E-mail: jfitzgerald@fas.harvard.edu

scending easterly and westerly jets (Baldwin et al. 2001). Laboratory models of non-rotating stratified turbulence in a reentrant annulus have also been shown to develop QBO-like banded jets (Plumb and McEwan 1978).

The analog of the β -plane system appropriate for modeling stacked jet formation in stratified turbulence is the stably stratified Boussinesq system. Like the β -plane system, the Boussinesq system does not generate turbulence spontaneously in the absence of an externally forced jet, so turbulence in these systems is traditionally maintained by a stochastic parameterization accounting for exogenous forcing of the turbulence. Numerical simulations of Boussinesq turbulence frequently develop strong vertically banded horizontal jets (Laval et al. 2003; Waite and Bartello 2004, 2006; Brethouwer et al. 2007; Marino et al. 2014; Rorai et al. 2015; Herbert et al. 2016; Kumar et al. 2017). These jets are known as vertically sheared horizontal flows (VSHFs), and develop in both 2D and 3D turbulence and in both non-rotating and weakly-rotating regimes. In previous work we showed that, in 2D stratified turbulence, VSHFs form via a statistical instability of homogeneous stratified turbulence in analogy with ZI (Fitzgerald and Farrell 2016). We refer to this instability, which belongs to a larger class of SSD instabilities alongside ZI, as VSHF instability (VSHFI).

Because the underlying instability is due to statistical organization of the turbulence, ZI and VSHFI have analytical expression in the SSD of turbulence, rather than in the dynamics of individual turbulent realizations. SSD refers to any theoretical approach to the analysis of fluctuating chaotic systems in which equations of motion are formulated directly for the statistical properties of the system rather than for the detailed system state. For example, the Fokker-Planck equation (FPE) is an SSD written for the time evolution of the probability density function of the state of any system whose realizations evolve according to a stochastic differential equation (SDE). The FPE is an exact SSD, so that the statistical predictions of the FPE correspond exactly to the statistics obtained by averaging over realizations of the SDE. However, for systems of practical interest the FPE cannot be solved numerically due to the extremely high dimension of its state space. Stochastic structural stability theory (S3T) (Farrell and Ioannou 2003) is an approximate SSD, closed at second order, that is amenable to numerical solution and theoretical analysis and is the basis of ZI and VSHFI.

Recent progress in the application of SSD has resulted from the realization that second-order closure of the SSD provides a good description of the dynamics of anisotropic turbulence dominated by large coherent structures. To obtain the second-order S3T closure, we decompose the dynamical variables of the flow into two components: a coherent component and an incoherent component. In the equations of motion of the coherent component all nonlinear interactions are kept intact. In the equations of mo-

tion of the incoherent component the nonlinear interactions between the coherent and incoherent components are retained, but the self-interactions of the incoherent component are not retained due to the status of S3T as a canonical second-order closure (Herring 1963). The dynamics of the incoherent component is then equivalent to linear evolution about the instantaneous coherent flow. The incoherent component feeds back on the coherent component via the Reynolds stresses and buoyancy fluxes. S3T is appropriate for analyzing turbulent systems in which the mechanisms of interest consist of spectrally nonlocal interactions between coherent large-scale structure and incoherent smaller scale turbulence. Absence of perturbation-perturbation nonlinearity in the incoherent component of the S3T dynamics precludes mechanisms based on a spectrally local turbulent cascade.

The state variables of S3T are the mean state of the turbulence (the first cumulant, which is the coherent component) and the covariance of the deviations from the mean state (the second cumulant, which is the incoherent component). The mean and the covariance interact quasi-linearly (QL) within the second-order closure due to the absence of the self-interactions of the deviations. S3T, and the related second-order closure referred to as CE2 (for second-order cumulant expansion) (Marston 2010), has been successfully applied to analyze many different turbulent systems that exhibit large-scale coherent structure. Even though nonlinearity is highly restricted in QL dynamics, the results of QL and S3T simulations have demonstrated that QL dynamics correctly reproduces the inhomogeneous structure of planetary turbulence (Farrell and Ioannou 2003, 2007, 2008, 2009b,a; Marston 2010, 2012; Srinivasan and Young 2012; Tobias and Marston 2013; Bakas and Ioannou 2013a; Constantinou et al. 2014; Bakas and Ioannou 2014; Constantinou et al. 2016; Farrell and Ioannou 2017b). These results indicate that QL dynamics accounts for the physical mechanisms responsible for the formation and maintenance of large-scale coherent structures in anisotropic turbulence. S3T has also been applied to analyze the interaction of turbulence with large-scale coherent structure in the drift wave-zonal flow plasma system (Farrell and Ioannou 2009; Parker and Krommes 2013), unstratified 2D flow (Bakas and Ioannou 2011), rotating magnetohydrodynamics (Tobias et al. 2011; Squire and Bhattarjee 2015), and the turbulence of stable ion-temperature-gradient modes in plasmas (St-Onge and Krommes 2017).

Zonal jet emergence in barotropic β -plane turbulence has been analyzed in particular depth using S3T. Early applications of S3T (Farrell and Ioannou 2003, 2007) showed that zonal jets form via the instability now referred to as ZI and that jet growth occurs through spectrally nonlocal transfers of energy from the perturbations into the jets, rather than through a spectrally local incoherent cascade. The analytical framework of S3T has since been

extended to enable analysis of the jet formation instability in unbounded turbulence using a physical-space representation (Srinivasan and Young 2012) as well as the emergence of non-zonal coherent structures (Bernstein and Farrell 2010; Bakas and Ioannou 2013a) and their coexistence with coherent zonal jets (Constantinou et al. 2016). The predictions of S3T and CE2 have been verified through comparison with fully nonlinear simulations (Tobias and Marston 2013; Bakas and Ioannou 2014; Constantinou et al. 2014). S3T has also been used to demonstrate that zonal jets can be analyzed within the mathematical and conceptual framework of pattern formation (Parker and Krommes 2014; Bakas et al. 2017). Of particular relevance to the present study, S3T has been applied to analyze the mechanism of ZI in great detail, including determining the contribution of specific physical processes, such as shear straining and Rossby wave propagation, to the positive and negative wave-mean flow feedbacks between the jet and the turbulent spectrum that underlie ZI (Bakas and Ioannou 2013b; Bakas et al. 2015).

Wave-mean flow feedbacks similar to those which underlie ZI have also been proposed as the drivers of vertically banded jets in stratified turbulence. In the case of the QBO, wave-mean flow interactions between the zonal flow and gravity waves propagating upward from the troposphere underpin the conventional theoretical explanation of the QBO (Holton and Lindzen 1972; Plumb 1977). In the case of the EDJs, a number of theoretical explanations have been suggested for their existence, including direct driving by surface winds (Wunsch 1977; McCreary 1984), an instability of finite-amplitude equatorial waves (Hua et al. 2008), and a nonlinear cascade of baroclinic mode energy into the equatorial region (Salmon 1982). However, recent realistic numerical simulations (Ascani et al. 2015) and earlier theoretical analysis (Muench and Kunze 1999) suggest that the EDJs instead result from wave-mean flow feedbacks. In the case of VSHFs in simulations of stratified turbulence, relatively few mechanisms have been proposed for their existence despite their ubiquity. A commonly advanced idea is that resonant and near-resonant interactions among gravity waves may play an important role (Smith 2001; Smith and Waleffe 2002). Recently, we have applied S3T to show that in 2D stratified turbulence the VSHF emerges as a result of an S3T instability analogous to ZI, and to analyze how the VSHF is equilibrated and maintained at finite amplitude (Fitzgerald and Farrell 2016).

Here we carry out an S3T analysis of VSHF emergence in 2D stratified turbulence that complements our previous work by taking advantage of the closed-form, linearized approach to analyzing S3T instabilities first developed by Srinivasan and Young (2012), hereafter SY12, in the context of ZI. This approach enables us to characterize VSHFI in terms of a closed-form dispersion relation for the instability growth rate in which the dependence on parameters

such as the stratification strength is explicit and which is amenable to asymptotic analysis. This approach also enables the application to VSHFI of the techniques first developed by Bakas and Ioannou (2013b) and Bakas et al. (2015), in the context of ZI, to analyze the VSHFI wave-mean flow feedback mechanism in detail. We use these analytical tools to determine the relationship between the properties of VSHFI and the structure of the underlying turbulence, and to determine the roles of various physical processes, such as gravity wave dynamics and shear straining of the vorticity field, in the VSHFI mechanism. S3T, and the closed-form linear approach in particular, allows these determinations to be made straightforwardly and with greater clarity than would be possible through interpretation of nonlinear simulations.

The rest of the paper is structured as follows. In Section 2 we introduce the fully nonlinear equations of motion (NL) for the 2D stochastically maintained Boussinesq system and its QL counterpart and show the results of example simulations illustrating the phenomenon of VSHF emergence and the degree to which the QL and S3T systems accurately capture the VSHF behavior. In Section 3 we formulate the S3T equations. In Section 4 we apply the closed-form linearized S3T approach to analyze the linear stability of homogeneous stratified turbulence and derive a dispersion relation for the growth rate of VSHFI. We also derive a dispersion relation for a related S3T instability governing the emergence of horizontal mean buoyancy layers (HMBLs) which we refer to as HMBLI. In Section 5 we apply these dispersion relations to analyze how VSHFI and HMBLI depend on the parameters and on the structure of the underlying turbulence. In Section 6 we analyze the stability boundary, or neutral curve, of VSHFI and compare the predictions of S3T to the results of NL simulations. In Sections 7 and 8 we analyze the wave-mean flow feedback mechanism of VSHFI and HMBLI in detail. We provide a summary and discussion in Section 9.

2. Emergence of Horizontal Mean Structure in 2D Stratified Turbulence

a. NL System

We study VSHF formation in 2D stably stratified Boussinesq turbulence maintained by homogeneous stochastic excitation. For our theoretical analysis we use a domain that is unbounded in both directions, and for our numerical simulations we use a doubly periodic domain of unit aspect ratio. Anticipating the formation of horizontal mean structure we write the equations of motion in Reynolds-decomposed form in which the averaging operator is the horizontal mean. The equations of motion of

the NL system are

$$\partial_t \zeta' = -U \partial_x \zeta' + \partial_{zz}^2 U \partial_x \psi' + \partial_x b' + \sqrt{\varepsilon} \xi^\zeta - r \zeta' + \nu \Delta \zeta' + \text{EENL}^\zeta, \quad (1)$$

$$\partial_t b' = -U \partial_x b' - (N_0^2 + \partial_z B) \partial_x \psi' + \sqrt{\varepsilon} \xi^b - r b' + \nu \Delta b' + \text{EENL}^b, \quad (2)$$

$$\partial_t U = -\partial_z \overline{u'w'} - r_m U + \nu \partial_{zz}^2 U, \quad (3)$$

$$\partial_t B = -\partial_z \overline{w'b'} - r_m B + \nu \partial_{zz}^2 B, \quad (4)$$

where EENL^ζ and EENL^b denote the eddy-eddy nonlinear terms in the perturbation vorticity and buoyancy equations which are produced by the advection of perturbations by perturbations and which are given by the expressions

$$\text{EENL}^\zeta \equiv - \left[J(\psi', \Delta \psi') - \overline{J(\psi', \Delta \psi')} \right], \quad (5)$$

$$\text{EENL}^b \equiv - \left[J(\psi', b') - \overline{J(\psi', b')} \right]. \quad (6)$$

Here x and z are the horizontal and vertical coordinates, $\Delta = \partial_{xx}^2 + \partial_{zz}^2$ is the Laplacian, $J(f, g) = (\partial_x f)(\partial_z g) - (\partial_z f)(\partial_x g)$ is the Jacobian, ψ is the streamfunction satisfying $(-\partial_z \psi, \partial_x \psi) = (u, w)$ where u and w are the horizontal and vertical velocity components, ζ is the vorticity defined as $\zeta = \partial_x w - \partial_z u = \Delta \psi$ and b is the buoyancy. We denote the horizontal mean operator by an overbar and perturbations from the mean by a prime. For convenience we denote the horizontal mean velocity and buoyancy by capital letters so that $\bar{u} \equiv U$ and $\bar{b} \equiv B$. The stochastic excitations of the perturbation vorticity and buoyancy fields are denoted by ξ^ζ and ξ^b .

The parameters of the system are the strength of the stochastic excitation, ε , the constant background buoyancy frequency, N_0^2 , the Rayleigh drag coefficients for the perturbations, r , and for the mean fields, r_m , and the viscosity, ν . Although fundamental studies of stratified turbulence typically do not include large-scale dissipation such as Rayleigh drag, we do so here both to connect our analysis more closely to the well-studied β -plane turbulence system, as well as to model the effects of turbulent dissipation by processes that are unresolved in our 2D system. Turbulent dissipation is conventionally parameterized as diffusive and therefore damps the large scales less strongly. As a simplified model of such scale-dependent dissipation we use different Rayleigh drag coefficients for the mean and perturbation fields, with the mean coefficient being the smaller of the two. We set the values of the dissipation parameters r , r_m , and ν , so that the buoyancy and velocity/vorticity fields are damped with equal strength, following standard practice in previous studies of VSHFs.

Viscosity is chosen to be small and is included to ensure numerical convergence.

To complete the formulation of the NL system it remains to specify the stochastic excitation. We analyze the conventionally studied case of turbulence maintained by statistically stationary white noise excitation with a prescribed covariance structure in space. The two-point, two-time covariance function of the vorticity excitation, ξ^ζ , is thus given by

$$\langle \xi_1^\zeta(t_i) \xi_2^\zeta(t_j) \rangle \equiv \delta(t_i - t_j) \Xi(\vec{x}_1, \vec{x}_2), \quad (7)$$

where we have introduced the notation $\xi_{1,2}^\zeta(t) = \xi^\zeta(\vec{x}_{1,2}, t)$. Similarly, we have

$$\langle \xi_1^b(t_i) \xi_2^b(t_j) \rangle \equiv \delta(t_i - t_j) \Theta(\vec{x}_1, \vec{x}_2), \quad (8)$$

$$\langle \xi_1^\zeta(t_i) \xi_2^b(t_j) \rangle \equiv \delta(t_i - t_j) G^\zeta(\vec{x}_1, \vec{x}_2), \quad (9)$$

$$\langle \xi_1^b(t_i) \xi_2^\zeta(t_j) \rangle \equiv \delta(t_i - t_j) G^b(\vec{x}_1, \vec{x}_2), \quad (10)$$

for the covariance of ξ^b and the covariances between ξ^ζ and ξ^b . The structure of the excitation in space is determined by the choice of the functions Ξ , Θ , G^ζ , and G^b (see Appendix D for a concrete example). In this work we use two excitation distributions: Isotropic ring excitation (IRE) in which the excitation injects energy into a narrow ring in wavenumber space, and monochromatic excitation (MCE) in which the excitation injects energy into a single horizontal wavenumber component with a Gaussian covariance structure in the vertical direction. Mathematical descriptions of IRE and MCE are provided in Section 5 and examples of realizations in physical space are shown in Figure 1. In all cases we choose the excitation to be statistically homogeneous so that Ξ , Θ , G^ζ and G^b depend on \vec{x}_1 and \vec{x}_2 only in the combination $\vec{x}_1 - \vec{x}_2$. We also note that, because the point labels \vec{x}_1 and \vec{x}_2 are arbitrary, the covariance functions obey the symmetry relations

$$\Xi(\vec{x}_1 - \vec{x}_2) = \Xi(\vec{x}_2 - \vec{x}_1), \quad (11)$$

$$\Theta(\vec{x}_1 - \vec{x}_2) = \Theta(\vec{x}_2 - \vec{x}_1), \quad (12)$$

$$G^\zeta(\vec{x}_1 - \vec{x}_2) = G^b(\vec{x}_2 - \vec{x}_1). \quad (13)$$

Figure 2 shows an example simulation of the NL system in which a VSHF forms. Equations (1)-(4) were solved in a doubly periodic domain of unit aspect ratio using the finite-difference fluid solver DIABLO (Taylor 2008) with a resolution of 512 grid points in the x and z directions. In dimensional units the domain size is $L = 1$ m and the parameters used are $r = 1 \text{ s}^{-1}$, $r_m = 0.1 \text{ s}^{-1}$, $N_0^2 = 10^3 \text{ s}^{-2}$, $\nu = 2.4 \times 10^{-5} \text{ m}^2 \text{ s}^{-1}$, $\varepsilon = 0.14 \text{ m}^2 \text{ s}^{-3}$. Turbulence is maintained with IRE centered on the ring of wavenumbers with $k_e/(2\pi) = 4\sqrt{2} \text{ m}^{-1}$. Figure 2 (a) shows a snapshot of the vorticity field after 60 s of spin up, illustrating the emergent vertical banding. The bands coincide with the

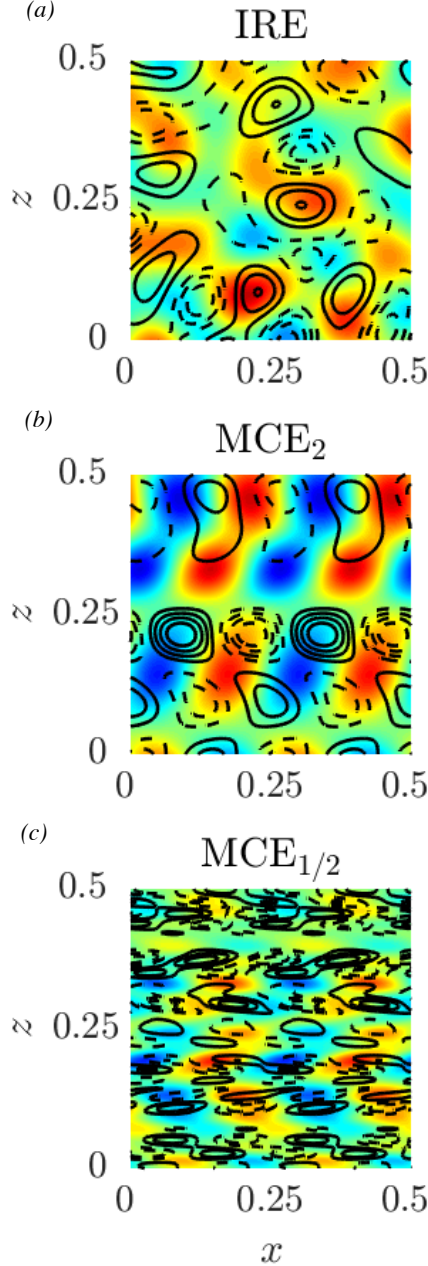


FIG. 1. Physical space realizations of the excitation structures IRE (a) and MCE (b,c). The domain is square and doubly periodic with linear dimension $L = 1$, and a quarter of the domain is shown. In this example, IRE excites perturbations in a narrow ring of wavenumbers centered at $k_e/(2\pi L) = 4$ and MCE excites the horizontal wavenumber component $k_0/(2\pi L) = 4$ with a Gaussian covariance structure in the vertical direction. The autocorrelation lengthscales for the MCE buoyancy excitation are $k_0\ell_c = 2$ (b) and $k_0\ell_c = 0.5$ (c). Colors (contours) show the buoyancy (vorticity) excitation.

shear regions of an energetic VSHF, U , the time evolution of which is shown in Figure 2 (b). The instantaneous buoyancy field, shown in Figure 2 (c), does not show obvious

vertical banding. However, time evolution of the horizontal mean buoyancy, B , reveals mean layered structures that are too weak to be visible in the instantaneous snapshots but are persistent over several mean damping times (Figure 2 (d)). We refer to such layered buoyancy structures as horizontal mean buoyancy layers (HMBLs).

Figure 3 (a) shows the time evolution of the kinetic energy of the VSHF and the total energy of the perturbations (the darkest curves show the behavior of the NL system). The perturbation kinetic, potential, and total energies are defined as

$$K' = [u'^2 + w'^2]/2, \quad V' = [b'^2]/2N_0^2, \quad E' = K' + V', \quad (14)$$

where square brackets indicate the domain average. The kinetic energy of the VSHF, the potential energy of the HMBLs, and the total energy of the horizontal mean state are defined as

$$\bar{K} = [U^2]/2, \quad \bar{V} = [B^2]/2N_0^2, \quad \bar{E} = \bar{K} + \bar{V}. \quad (15)$$

In the absence of excitation and dissipation the total energy, $E = \bar{E} + E'$, is conserved. The VSHF energy grows approximately exponentially in time before approaching a quasi-steady state in which the VSHF is energetically dominant, weakly fluctuating, and slowly varying in association with the slow variations in the structure of U in Figure 2 (b). Figure 3 (b) shows how the VSHF and perturbation energies depend on the nondimensional excitation strength, $\varepsilon k_e^2/r^3$, as measured by the zonal mean flow index,

$$\text{zmf} \equiv \bar{K}/E, \quad (16)$$

which gives the fraction of the total energy that is contained in the VSHF. The zmf is small for $\varepsilon \lesssim 50$, with nearly all the energy being contained in the perturbation field. As ε is increased beyond this threshold value, the zmf increases sharply. This transition in behavior coincides with the emergence of a coherent VSHF.

We will show that the sudden emergence of the VSHF as the excitation strength is increased results from a bifurcation associated with the VSHFI growth rate crossing zero toward positive values at a critical excitation strength. This bifurcation, which is explicitly predicted in the SSD, is reflected in the NL system as shown in Figure 3 (b). We next develop the SSD framework necessary for analyzing VSHFI.

b. QL System

Before developing the S3T implementation of SSD it is useful to first develop the QL system. The QL system is an approximation to the NL system in which the EENL terms are discarded from the perturbation dynamics (1)-(2) so

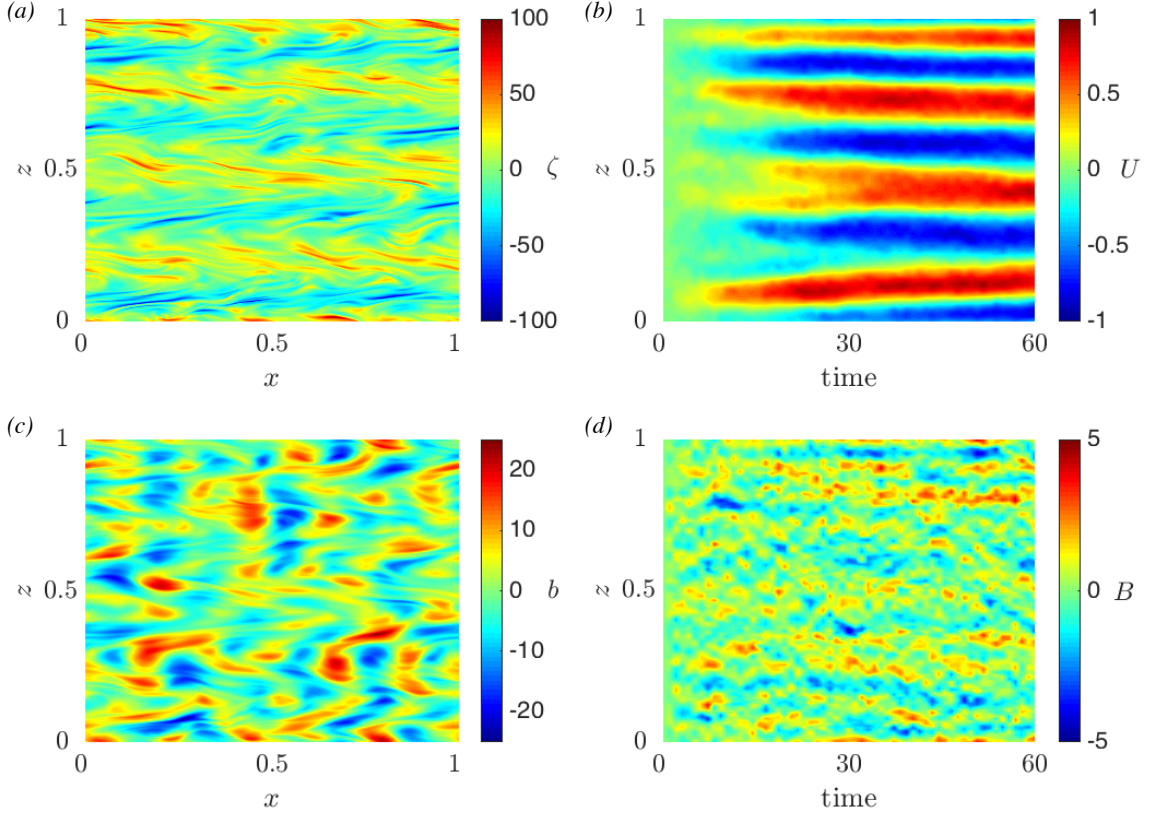


FIG. 2. Emergence of a VSHF in the NL system in which turbulence is maintained with IRE. Panels show (a) the final state of the vorticity field, (b) the time evolution of the horizontal mean velocity, (c) the final state of the buoyancy field, and (d) the time evolution of the horizontal mean buoyancy. The NL system spontaneously develops vertical banding in the vorticity field associated with the development of a strong VSHF. The buoyancy is also organized into more unsteady layered structures that are not apparent in snapshots but are revealed by horizontal averaging. For comparison with the results of Section 5, the nondimensional parameters used are $\varepsilon = 177$, $N_0^2 = 10^3$, $r_m = 0.1$, and $\nu = 0.03$, and the nondimensional wavenumber of the emergent VSHF is $m = 1/\sqrt{2}$. Dimensional parameters and simulation details can be found in the text.

that nonlinearity is confined to wave-mean flow interactions. The QL perturbation dynamics are

$$\partial_t \zeta' = -U \partial_x \zeta' + \partial_z^2 U \partial_x \psi' + \partial_x b' + \sqrt{\varepsilon} \xi \zeta' - r \zeta' + \nu \Delta \zeta', \quad (17)$$

$$\partial_t b' = -U \partial_x b' - (N_0^2 + \partial_z B) \partial_x \psi' + \sqrt{\varepsilon} \xi b' - r b' + \nu \Delta b'. \quad (18)$$

Perturbation equations (17)-(18) are then coupled to the mean equations (3)-(4) to produce the closed QL system.

The QL system implies a hypothesis about which aspects of the dynamics are essential to large-scale organization and which are inessential. To the extent that wave-mean flow interactions are the primary drivers of VSHF formation, the QL system should capture the behavior of the NL system in the VSHF-forming regime. Conversely, if arrest of an upscale turbulent cascade at the VSHF scale were mechanistically responsible for the formation of VSHFs then there would be no agreement between NL simulations and QL simulations because the nonlinear interaction among perturbations has been eliminated in QL.

The dark grey curves in Figure 3 compare the behavior of the QL system to that of the NL system for the chosen example case. The QL system shows good agreement with the NL system, indicating that the dynamical approximations underlying the QL system retain the mechanism responsible for VSHF emergence. That VSHF formation does not result from a traditional spectrally local inverse cascade has previously been noted by Smith and Waleffe (2002).

c. S3T System

The S3T system is a turbulent closure at second order and so necessarily has the form of QL dynamics (Herring 1963). The analytical simplicity of S3T results from making the ergodic assumption that the horizontal average, which is the appropriate choice of mean for the purpose of analyzing VSHF dynamics, is equivalent to the ensemble average over realizations of the stochastic excitation.

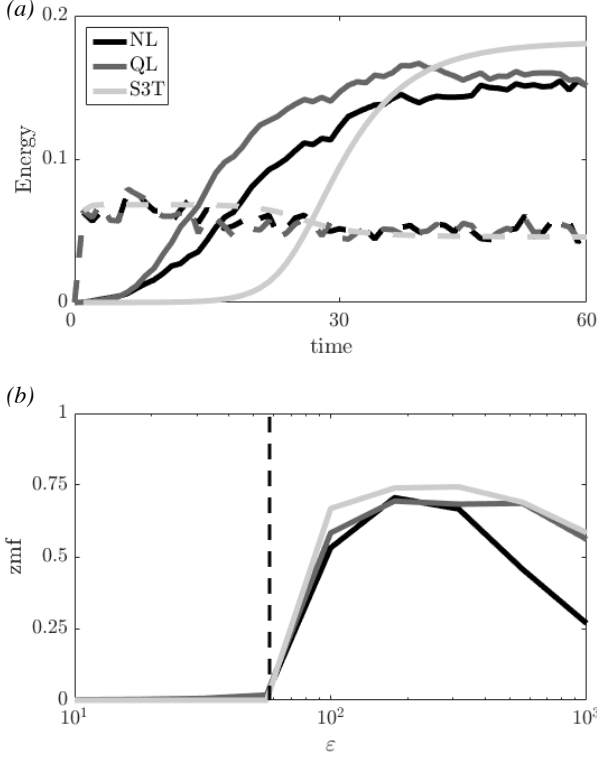


FIG. 3. Comparison of VSHF emergence diagnostics in simulations of the NL, QL, and S3T systems. Parameters and numerical details are as in Figure 2 unless otherwise specified. Panel (a) shows the dimensional total energy of the perturbation field (dashed) and the dimensional kinetic energy of the VSHF (solid) as functions of time for nondimensional excitation strength $\varepsilon = 177$. Panel (b) shows the fraction of the total energy contained in the VSHF after a spin-up period as a function of ε . The S3T system captures the behavior of the NL and QL systems, and each system exhibits approximately exponential growth of VSHF energy in time (a) and abrupt growth in VSHF energy as ε is increased beyond a critical threshold value (b).

This ergodic assumption allows the dynamics of the second cumulant to be expressed in the analytical form of a time-dependent Lyapunov equation. The ergodic approximation is justified when the domain has sufficient horizontal extent to permit many approximately independent perturbation structures, such as in the case of Figure 2 (a) in which several perturbation features are visible at each height.

Derivations of the S3T system are provided in Section 3, following the SY12 approach in continuous variables, and in Appendix A, following the conventional matrix approach of Farrell and Ioannou (2003). The two approaches are complementary mathematical formulations of the SSD. The continuous approach is useful for carrying out linear stability analysis and for deriving closed-form dispersion relations for instability growth rates that are amenable to asymptotic analysis. The matrix approach is required to analyze the finite-amplitude structure and

equilibration dynamics of the VSHF following its initial emergence.

The light grey curves in Figure 3 show the behavior of the matrix S3T system. Numerical details of the S3T solutions can be found in Appendix A. The VSHF emergence diagnostics in S3T are in good general agreement with those of the NL and QL systems. However, two aspects of the behavior of the S3T system differ from the behavior of the NL and QL systems. The first, visible in Figure 3 (a), is that the S3T VSHF takes longer to reach equilibrium than the NL and QL VSHFs. This results from the absence of noise in the S3T system which is present in the NL and QL systems. Because S3T is a deterministic and autonomous dynamical system in which VSHF formation occurs via a linear instability, the time at which the VSHF reaches equilibrium in S3T depends on the size of the small perturbations included in the initial conditions. A second aspect of the behavior of S3T that differs from that of NL and QL is that S3T exhibits an exact bifurcation structure in which the zmf is exactly zero below the critical excitation strength and sharply increases beyond it, whereas the NL and QL zmf's have small but nonzero values prior to the bifurcation point (Figure 3 (b)). The nonzero values of the zmf prior to the bifurcation point in NL and QL result from the excitation of weakly damped VSHF modes by the stochastic fluctuations in those systems (Constantinou et al. 2014). The vertical dashed line in Figure 3 (b) shows the VSHF bifurcation point predicted by the S3T dispersion relation derived in Section 5. This prediction is in good agreement with the results of the NL and QL systems and corresponds exactly with the behavior of the matrix S3T system.

3. S3T Equations of Motion

We now develop the S3T equations of motion following the SY12 approach. The dynamical variables characterizing the perturbation field in S3T are the two-point equal-time ensemble mean perturbation covariance functions. For example, the vorticity covariance is defined as

$$Z(\vec{x}_1, \vec{x}_2, t) \equiv \langle \zeta'_1(t) \zeta'_2(t) \rangle, \quad (19)$$

and the other required covariances are

$$\Psi \equiv \langle \psi'_1 \psi'_2 \rangle, \quad T \equiv \langle b'_1 b'_2 \rangle, \quad (20)$$

$$\Gamma^\zeta \equiv \langle \zeta'_1 b'_2 \rangle, \quad \Gamma^b \equiv \langle b'_1 \zeta'_2 \rangle, \quad (21)$$

$$S^\zeta \equiv \langle \psi'_1 b'_2 \rangle, \quad S^b \equiv \langle b'_1 \psi'_2 \rangle. \quad (22)$$

The covariances $\Gamma^{\zeta, b}$ and $S^{\zeta, b}$ are related through $\Gamma^\zeta = \Delta_1 S^\zeta$ and $\Gamma^b = \Delta_2 S^b$, where $\Delta_i \equiv \partial^2 / \partial x_i^2 + \partial^2 / \partial z_i^2$. We define them separately for convenience. Similar to equation (13) for the excitation cross-covariances, G^ζ and G^b , the perturbation cross-covariances, $\Gamma^{\zeta, b}$ and $S^{\zeta, b}$, obey the symmetry relations

$$\Gamma^\zeta(\vec{x}_1, \vec{x}_2) = \Gamma^b(\vec{x}_2, \vec{x}_1), \quad S^\zeta(\vec{x}_1, \vec{x}_2) = S^b(\vec{x}_2, \vec{x}_1). \quad (23)$$

Equations of motion for Z , T , and Γ^ζ can be derived straightforwardly from the QL system using the ergodic approximation. Details are provided in Appendix B. We express the dynamics using the collective coordinates

$$x = x_1 - x_2, \quad z = z_1 - z_2, \quad (24)$$

$$\bar{x} = (x_1 + x_2)/2, \quad \bar{z} = (z_1 + z_2)/2. \quad (25)$$

Assuming that the turbulence is statistically homogeneous in the horizontal direction, as suggested by Figure 2 (a), we take all covariances to be independent of \bar{x} . Covariances may, however, depend on \bar{z} , because the emergent vertical banding breaks the homogeneity of the turbulence in the vertical direction. The covariance dynamics are

$$\partial_t Z + (U_1 - U_2) \partial_x Z + (U_1'' + U_2'') \partial_{xz}^3 \Psi - (U_1'' - U_2'') (\Delta + \frac{1}{4} \partial_{zz}^2) \partial_x \Psi = -2rZ + \partial_x (\Gamma^b - \Gamma^\zeta) + \varepsilon \Xi, \quad (26)$$

$$\partial_t T + (U_1 - U_2) \partial_x T + N_0^2 \partial_x (S^\zeta - S^b) + B_1' \partial_x S^\zeta - B_2' \partial_x S^b = -2rT + \varepsilon \Theta, \quad (27)$$

$$\partial_t \Gamma^\zeta + (U_1 - U_2) \partial_x \Gamma^\zeta - U_1'' \partial_x S^\zeta - (N_0^2 + B_2') (\Delta + \partial_{zz}^2 + \frac{1}{4} \partial_{zz}^2) \partial_x \Psi = -2r\Gamma^\zeta + \partial_x T + \varepsilon G^\zeta, \quad (28)$$

where U_i'' denotes the curvature of U at z_i and we now use $\Delta = \partial_{xx}^2 + \partial_{zz}^2$ to denote the Laplacian in the difference coordinates. The equation of motion for Γ^b can be obtained from (28) using (23). Viscous terms included to ensure numerical convergence in NL and QL simulations are excluded from the present development for simplicity but can be straightforwardly included.

To obtain a closed dynamics, the equations of motion for U and B must also be expressed in terms of the perturbation covariances. The turbulent momentum and buoyancy fluxes can be written as (see Appendix B)

$$\langle u'w' \rangle = \partial_{xz}^2 \Psi \Big|_{x=z=0}, \quad \langle w'b' \rangle = \frac{1}{2} \partial_x (S^\zeta - S^b) \Big|_{x=z=0}. \quad (29)$$

The dynamics of U and B then become

$$\partial_t U = -r_m U - \partial_{xz}^3 \Psi \Big|_{x=z=0}, \quad (30)$$

$$\partial_t B = -r_m B - \frac{1}{2} \partial_{xz}^2 (S^\zeta - S^b) \Big|_{x=z=0}. \quad (31)$$

Equations (26)-(28) together with (30)-(31) constitute the closed S3T system.

Before proceeding to the analysis of S3T it is useful to express aspects of the energetics in terms of covariances. The ensemble mean values of K' and V' are given by

$$\langle K' \rangle = -\frac{1}{2} (\Delta - \frac{1}{4} \partial_{zz}^2) \Psi \Big|_{x=z=0}, \quad \langle V' \rangle = \frac{1}{2} N_0^{-2} T \Big|_{x=z=0}. \quad (32)$$

From (26)-(27), the rates at which kinetic and potential energy are injected into the perturbation field by the stochastic excitation are

$$\varepsilon_K = -\frac{\varepsilon}{2} \Delta^{-1} \Xi \Big|_{x=z=0}, \quad \varepsilon_V = \frac{\varepsilon}{2N_0^2} \Theta \Big|_{x=z=0}. \quad (33)$$

The excitation strength control parameter, ε , and the excitation structure functions, Ξ and Θ , collectively determine the overall amplitude of the excitation, its spatial structure, and how the injected energy is partitioned between kinetic and potential forms. We choose the convention that the functions Ξ and Θ set the spatial structure of the excitation and the ratio $\varepsilon_K/\varepsilon_V$, while the control parameter ε scales the total energy injection rate, $\varepsilon_K + \varepsilon_V$. We further choose to normalize the functions Ξ and Θ such that the total energy injection rate is equal to the value of the parameter ε , so that $\varepsilon_K + \varepsilon_V = \varepsilon$.

It is useful to express ε_K and ε_V in terms of the Fourier transforms of the excitation covariances. Using the Fourier conventions

$$f(\vec{x}) = \iint \frac{dpdq}{(2\pi)^2} \tilde{f}(\vec{p}) e^{i\vec{p} \cdot \vec{x}}, \quad \tilde{f}(\vec{p}) = \iint dx dz f(\vec{x}) e^{-i\vec{p} \cdot \vec{x}}, \quad (34)$$

with $\vec{p} = (p, q)$ and $h^2 = p^2 + q^2$, we have

$$\varepsilon_K = \varepsilon \iint \frac{dpdq}{(2\pi)^2} \frac{\tilde{\Xi}}{2h^2} \equiv \varepsilon \iint \frac{dpdq}{(2\pi)^2} \tilde{K}(p, q), \quad (35)$$

$$\varepsilon_V = \varepsilon \iint \frac{dpdq}{(2\pi)^2} \frac{\tilde{\Theta}}{2N_0^2} \equiv \varepsilon \iint \frac{dpdq}{(2\pi)^2} \tilde{V}(p, q), \quad (36)$$

$$\varepsilon = \varepsilon_K + \varepsilon_V \equiv \varepsilon \iint \frac{dpdq}{(2\pi)^2} \tilde{E}(p, q), \quad (37)$$

where we have defined the functions $\tilde{K} = \tilde{\Xi}/(2h^2)$, $\tilde{V} = \tilde{\Theta}/(2N_0^2)$, and $\tilde{E} = \tilde{K} + \tilde{V}$ which characterize the spectral structures of the kinetic, potential, and total energy injection rates. In our normalization the integral in (37) is equal to 1, as \tilde{E} controls the spectral distribution of the excitation but not its total energy injection rate.

4. S3T Stability of Homogeneous Stratified Turbulence

We next apply S3T to analyze the possibility of emergent vertical banding such as that observed in Figure 2. We begin by considering the alternate possibility that no coherent structures exist and that the turbulence is statistically steady and homogeneous. S3T admits a fixed point solution corresponding to such a homogeneous state. We analyze the linear stability of this solution to determine the rates of growth or decay of perturbations to homogeneous turbulence associated with VSHFs and HMBLs. If perturbations with positive growth rates exist, the underlying homogeneous turbulence is unstable to the development of vertical banding, which provides an explanation for the initial emergence of structure as observed in simulations.

Statistically steady homogeneous turbulence is characterized by $U = B = \partial_t = \partial_z = 0$. Homogeneous S3T equilibria, whose covariance functions are indicated by a subscript H , obey the linear equations

$$0 = -2rZ_H + \partial_x(\Gamma_H^b - \Gamma_H^\zeta) + \varepsilon\Xi, \quad (38)$$

$$0 = -N_0^2\partial_x(S_H^\zeta - S_H^b) - 2rT_H + \varepsilon\Theta, \quad (39)$$

$$0 = N_0^2\partial_x\Delta\Psi_H - 2r\Gamma_H^\zeta + \partial_x T_H + \varepsilon G^\zeta. \quad (40)$$

Equations (38)-(40) can be solved for general Ξ , Θ , and G^ζ . However, a great simplification occurs when the excitation is chosen such that the potential and kinetic energy injection rates are equal to one another at each wavenumber and also such that the excitations of the vorticity and buoyancy fields are uncorrelated with one another. These conditions correspond to the relations

$$\tilde{K} = \tilde{V} = \frac{1}{2}\tilde{E}, \quad G^\zeta = G^b = 0. \quad (41)$$

The excitation structures shown in Figure 1 have these fairly natural properties. When (41) holds, the solution of (38)-(40) is given by

$$Z_H = \frac{\varepsilon\Xi}{2r}, \quad T_H = \frac{\varepsilon\Theta}{2r}, \quad \Gamma_H^{\zeta,b} = S_H^{\zeta,b} = 0, \quad (42)$$

which can be interpreted as a fluctuation-dissipation relation. We note that the fixed point solution (42) does not depend on N_0^2 . An analogous result has been obtained for β -plane turbulence, in which the homogeneous turbulent state does not depend on β (Srinivasan and Young 2012).

We now outline the linear stability analysis of the fixed point (42). Details are provided in Appendix C. We begin by expanding the perturbation covariances to first-order about the fixed point as $Z(x, z, \bar{z}, t) = Z_H(x, z) + \delta Z(x, z, \bar{z}, t)$ and similarly for T , Γ^ζ , and Γ^b . Horizontal mean structures are expanded about zero as $U(\bar{z}, t) = \delta U(\bar{z}, t)$ and $B(\bar{z}, t) = \delta B(\bar{z}, t)$. Substitution into (26)-(31)

then yields a set of linearized equations such as

$$\begin{aligned} \partial_t \delta Z + (\delta U_1 - \delta U_2) \partial_x Z_H - (\delta U_1'' - \delta U_2'') \Delta \partial_x \Psi_H \\ - \partial_x (\delta \Gamma^b - \delta \Gamma^\zeta) = -2r \delta Z, \end{aligned} \quad (43)$$

which governs the perturbation to the vorticity covariance. It is then useful to write the perturbation variables in the Fourier ansatz

$$\delta C(x, z, \bar{z}, t) = e^{st} e^{im\bar{z}} \hat{C}(x, z)_{m,s}, \quad (44)$$

$$\delta U(\bar{z}, t) = e^{st} e^{im\bar{z}} \hat{U}_{m,s}, \quad (45)$$

$$\delta B(\bar{z}, t) = e^{st} e^{im\bar{z}} \hat{B}_{m,s}, \quad (46)$$

plus complex conjugate terms, where C is a placeholder for Z , T , Γ^ζ , and Γ^b . The perturbation covariance coefficients, $\hat{C}(x, z)$, are further decomposed using their Fourier transforms as in (34). Following these manipulations we obtain an eigenproblem for the eigenvalue, s , whose real part is equal to the growth rate of banded perturbations with vertical wavenumber m in homogeneous turbulence.

The eigenproblem simplifies dramatically when the excitation structure is chosen to have the reflection symmetry $\tilde{E}(p, q) = \tilde{E}(-p, q)$, which corresponds to equal excitation of gravity wave modes with positive and negative phase speeds. This property is typical of excitation structures chosen in theoretical studies of stratified turbulence and is possessed by the excitation structures shown in Figure 1. For reflection-symmetric excitation, the eigenproblem for s factors into two decoupled eigenproblems, each of which determines a set of modes and their growth rates. The first set of modes, which we call the VSHF modes, has $\delta B = 0$ so that the horizontal mean structure consists purely of a VSHF perturbation with no HMBL perturbation. The second set of modes, which we call the HMBL modes, has $\delta U = 0$ so that the horizontal mean structure is a pure HMBL perturbation. Each set of modes has its own dispersion relation. Denoting by s_U the eigenvalues corresponding to the VSHF modes and by s_B the eigenvalues corresponding to the HMBL modes, the dispersion relations are

$$\frac{\bar{s}_U}{s'_U} = \varepsilon \int dp dq \mathcal{F}_U(p, q, m, N_0^2, r, s_U) \tilde{E}(p, q), \quad (47)$$

$$\frac{\bar{s}_B}{s'_B} = \varepsilon \int dp dq \mathcal{F}_B(p, q, m, N_0^2, r, s_B) \tilde{E}(p, q), \quad (48)$$

where $\bar{s}_{U,B} = s_{U,B} + r_m$ and $s'_{U,B} = s_{U,B} + 2r$. \mathcal{F}_U and \mathcal{F}_B are functions whose detailed forms are provided in Appendix C. Equations (47)-(48) are resistant to analytical solution because the eigenvalues, s_U and s_B , appear in the integrands. However, the eigenvalues can be computed numerically and approximate analytical solutions can be obtained in a variety of cases. In the next section we apply (47)-(48) to analyze the stability of homogeneous turbulence maintained by the IRE and MCE structures discussed in Section 2.

5. Application of the Dispersion Relations to the Cases of IRE and MCE

a. Isotropic Ring Excitation (IRE)

We first analyze VSHFI and HMBLI in stratified turbulence maintained by IRE. Nondimensionalizing length by the excitation scale, $1/k_e$, and time by the perturbation damping time, $1/r$, the energy injection spectrum is given by

$$\tilde{E}_{IRE}(p, q) = 2\pi\delta(h - 1). \quad (49)$$

Figure 1 (a) shows a realization in physical space of an excitation approximating (49). The IRE dispersion relations are obtained by evaluating (47)-(48) for $\tilde{E} = \tilde{E}_{IRE}$ (see Appendix D). Figure 4 (a) shows how s_U and s_B vary with m , the vertical wavenumber of the emergent banding, for several representative N_0^2 values¹. The parameters used are $\varepsilon = 75$, chosen so that $s_U > 0$ over some band of m for each selected value of N_0^2 , and $r_m = 0.1$, chosen to make contact with the simulations shown in Figures 2 and 3 and with our previous work (Fitzgerald and Farrell 2016).

The properties of VSHFI depend on the stratification. Setting the notation $s_U^* = \max_m[s_U(m)] = s_U(m^*)$, under weak stratification (Figure 4 (a), light solid curve), the fastest-growing VSHF corresponds to $m^* \approx 1$, and s_U^* is only weakly positive. VSHFs with $0 < m \lesssim 1$ have negative growth rates but decay more slowly than the explicit VSHF damping rate, *i.e.*, $-r_m < s_U < 0$. This indicates that relatively large-scale VSHFs are reinforced by IRE turbulence. VSHFs with $m \gtrsim 1$ have $s_U < -r_m$, indicating that relatively small-scale VSHFs are dissipated by IRE turbulence.

For small N_0^2 , VSHFI can be understood by perturbing about the case of unstratified IRE turbulence (see Appendix D). For $N_0^2 = 0$, the induced momentum flux, $\langle u'w' \rangle$, vanishes when the VSHF scale is larger than the excitation scale, so that $s_U = -r_m$ for $0 \leq m \leq 1$. For perturbatively weak stratification, s_U is modified to

$$s_U \approx -r_m + \frac{\varepsilon m^2 N_0^2}{8(2 - r_m)^3}, \quad (50)$$

which is valid for $0 < m < 1$. The estimate (50) is compared to the result from (47), and to the $N_0^2 = 0$ solution, in Figure 5. Quadratic enhancement of s_U as a function of m leads to $m^* = 1$ for weak stratification. Figure 4 (a) shows that $m^* \approx 1$ also corresponds to the fastest-growing VSHF at the intermediate stratification $N_0^2 = 10$. For $m > 1$ equation (50) is replaced by a more complex expression but the details are inessential due to the strong dissipation of these VSHFs by the zeroth order unstratified turbulence.

¹We note that for the parameters considered in Figure 4, s_U and s_B are real. Although the eigenvalues can be complex under some circumstances, we have found through experimentation that these cases do not typically correspond to the most unstable modes and as such we treat the case of real eigenvalues throughout this paper.

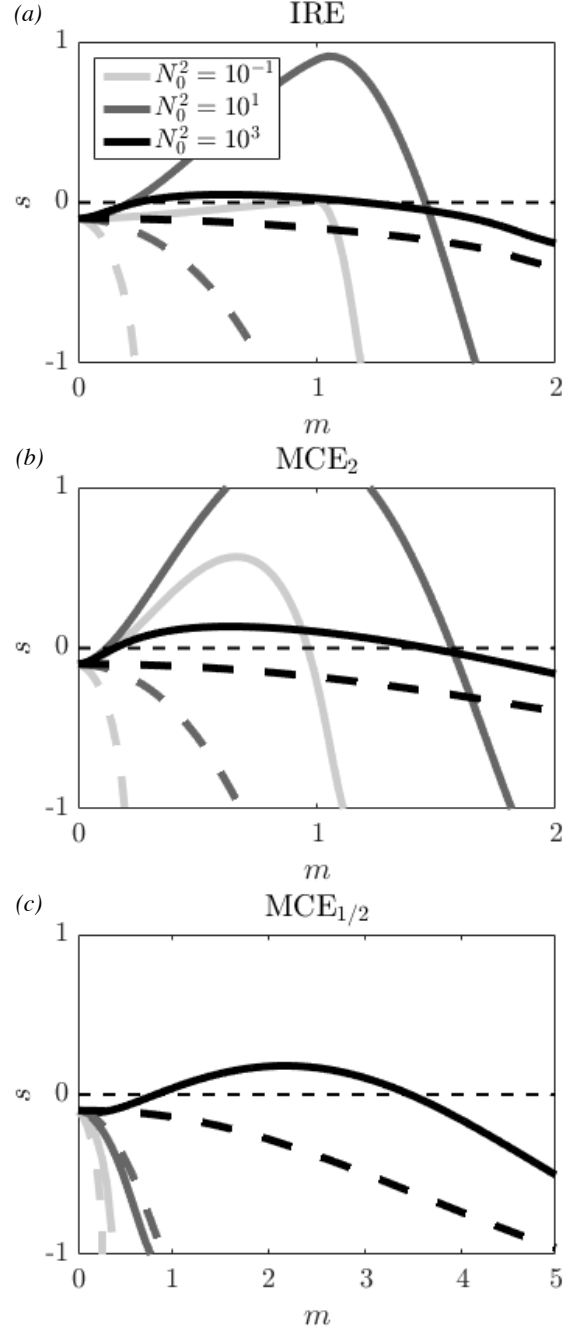


FIG. 4. VSHFI (solid) and HMBLI (dashed) growth rates as functions of the vertical wavenumber, m , of the horizontal mean structure for turbulence excitation structures (a) IRE, (b) MCE₂, and (c) MCE_{1/2}. Three representative N_0^2 values are shown: $N_0^2 = 10^{-1}$ (weak stratification, light curves), $N_0^2 = 10^1$ (intermediate stratification, medium curves), and $N_0^2 = 10^3$ (strong stratification, darkest curves). The parameters used are $\varepsilon = 75$, $r_m = 0.1$, and $\nu = 0$.

The quadratic increase of s_U with m in (50) suggests that VSHFI results from negative eddy viscosity. Indeed,

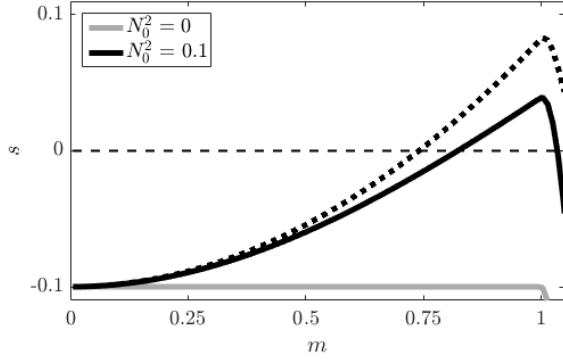


FIG. 5. VSHFI growth rate as a function of m under zero and weak stratification in the case of IRE. The light grey curve shows $s_U(N_0^2 = 0)$ and the solid black curve shows how s_U is enhanced when weak stratification is introduced. The thick dashed curve shows the asymptotic approximation (50). The parameters used are $\varepsilon = 50$, $r_m = 0.1$ and $\nu = 0$.

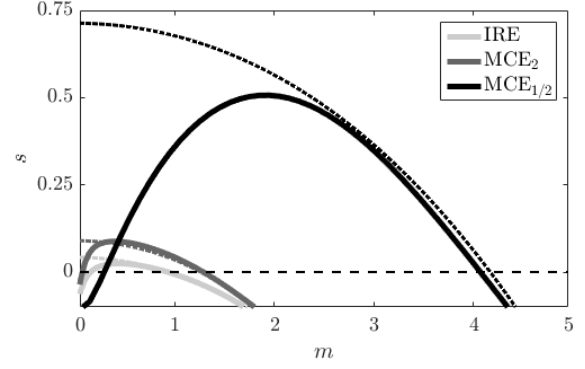


FIG. 6. VSHFI growth rates under strong stratification for the IRE, MCE_2 , and $MCE_{1/2}$ cases. Solid curves show growth rates calculated using the full dispersion relation and dashed curves show asymptotic approximations (see Appendices D and E). The structure of s_U is generic, with the fastest growing wavenumber approaching $m = 0$ as $N_0^2 \rightarrow \infty$. The parameters used are $\varepsilon = 50$, $N_0^2 = 10^5$, $r_m = 0.1$, and $\nu = 0$.

for $m \ll 1$, (47) gives

$$s \approx -r_m - v_{\text{eddy}} m^2, \quad (51)$$

$$v_{\text{eddy}} = -\varepsilon g(N_0^2, r_m), \quad (52)$$

where g is a positive-definite function (see Appendix D) so that $v_{\text{eddy}} < 0$ for all N_0^2 . We analyze the dynamics leading to $v_{\text{eddy}} < 0$ in Sections 7 and 8. In IRE β -plane turbulence, large-scale jets instead initially form due to negative eddy hyperviscosity (Srinivasan and Young 2012).

Both s_U^* and m^* are significantly modified as N_0^2 is increased. The value of s_U^* increases to a maximum near $N_0^2 = 10$ (Figure 4 (a)). As the stratification becomes strong, (47) gives (see Appendix D)

$$s_U \approx -r_m + (\varepsilon/N_0^2)(1 - r_m/2)(3 - m^2), \quad (53)$$

which is compared to the unapproximated result in Figure 6 (light grey curve) for $N_0^2 = 10^5$. The behavior of s_U is captured by (53) when m is not small. When m is small, the behavior of s_U is instead captured by (51). As N_0^2 increases, (53) indicates that the growth rate of VSHFI weakens ($s_U^* \rightarrow -r_m$) and the VSHF emerges at larger and larger scale ($m^* \rightarrow 0$). Similar results are found for ZI, with the jet growth rate weakening and the jet scale increasing as $\beta \rightarrow \infty$. This behavior is attributed to disruption of wave-mean flow interaction between travelling waves and stationary jets by the increase in Rossby wave group velocity (Bakas et al. 2015). This mechanism likely operates in stratified turbulence as well, with the increasing group velocity of gravity waves at large N_0^2 disrupting the wave-mean flow interaction underlying VSHFI.

The dashed curves in Figure 4 (a) show how the HMBLI growth rate, s_B , varies with m . In all cases shown, $s_B <$

$-r_m$, indicating that perturbations to homogeneous turbulence associated with HMBLs are dissipated by down-gradient eddy buoyancy fluxes. Although this result appears to contradict the results of the NL simulation shown in Section 2, which forms HMBLs, our previous work has shown that these HMBLs do not emerge in homogeneous turbulence but instead form nonlinearly once a finite-amplitude VSHF has emerged (Fitzgerald and Farrell 2016).

b. Monochromatic Excitation (MCE)

VSHFI occurs in stratified turbulence for a wide range of parameter choices and excitation structures, but the properties of VSHFI can depend on the properties of the excitation. To demonstrate this we analyze VSHFI in turbulence maintained by MCE, which is a red-noise structure that differs qualitatively from IRE while retaining comparable analytical simplicity. MCE excites a single horizontal wavenumber component, k_0 , with a Gaussian energy injection spectrum in vertical wavenumber. Nondimensionalizing² length by the horizontal scale of the excitation, $1/k_0$, and time by the perturbation damping time, $1/r$, the MCE energy injection spectrum is given by

$$\tilde{E}_{MCE}(p, q) = \pi^{3/2} \ell_c \exp(-\ell_c^2 q^2/4) [\delta(p+1) + \delta(p-1)]. \quad (54)$$

The parameter ℓ_c is equal to the correlation length of the excitation in the vertical direction and sets the width of the spectrum in the vertical wavenumber, q . We analyze the cases MCE_2 , with $\ell_c = 2$, and $MCE_{1/2}$, with $\ell_c = 1/2$, and compare them to the case of IRE. Physical-space realizations of MCE_2 and $MCE_{1/2}$ are shown in Figures 1 (b)

²Although our nondimensionalizations for the IRE and MCE cases differ slightly, results in the various cases can be directly compared for the same parameters when the ring wavenumber, k_e , is set equal to the MCE wavenumber, k_0 .

and (c). MCE_2 excites structures with somewhat greater vertical extent than horizontal extent, while $\text{MCE}_{1/2}$ excites structures with comparable or smaller vertical extent than horizontal extent.

The VSHFI and HMBLI dispersion relations for MCE are obtained by evaluating (47)-(48) with $\tilde{E} = \tilde{E}_{\text{MCE}}$ (see Appendix E). The growth rates, s_U and s_B , are shown in Figure 4 (b) and (c) for MCE_2 and $\text{MCE}_{1/2}$ as functions of the vertical wavenumber, m , of the emergent banding.

For small N_0^2 (light grey curves in Figure 4) the VSHFI properties differ markedly between the three excitation structures. Although VSHFI is weak for IRE as expressed by (50), s_U remains positive as $N_0^2 \rightarrow 0$ for MCE_2 and remains strongly negative as $N_0^2 \rightarrow 0$ for $\text{MCE}_{1/2}$. These results are consistent with previous work on unstratified turbulence by Bakas and Ioannou (2011) using a slightly modified formulation of MCE.

As N_0^2 is increased, the IRE and MCE_2 cases behave similarly, with s_U^* increasing to a maximum near $N_0^2 = 10$ before decaying like $1/N_0^2$. The $\text{MCE}_{1/2}$ case behaves quite differently, with $s_U^* < 0$ for weak and intermediate stratification values and $s_U^* > 0$ first occurring for $N_0^2 \approx 10^2$. Figure 6 compares s_U across the cases for $N_0^2 = 10^5$. The asymptotic behavior of s_U as $N_0^2 \rightarrow \infty$ is generic among the cases, but the band of wavenumbers for which the VSHF is supported by the eddy fluxes, as well as the maximum VSHF growth rate, differs between the cases. Surprisingly, the $\text{MCE}_{1/2}$ case exhibits the strongest VSHFI among all cases for large N_0^2 , with the VSHF emerging at the smallest vertical scale. We analyze the mechanism responsible for these properties in Sections 7 and 8.

The dashed curves in Figures 4 (b) and (c) show the HMBLI growth rate, s_B , for MCE. As was found for IRE, $s_B < 0$ in all cases shown. The failure of HMBLI to obtain positive growth rates for either canonical ring or red-noise excitation suggests that the initial formation of HMBLs is unlikely to arise from an instability of the homogeneous turbulence.

6. Stability boundaries

a. IRE

The dependence of VSHFI on the control parameters and excitation structure can be visualized clearly in terms of the stability boundary or neutral curve. The stability boundary is defined as the critical value of ε , denoted ε_c , at which s_U first becomes positive as ε is increased. When the emergent VSHF is stationary so that s_U is real, the stability boundary coincides with the simultaneous conditions $s_U = 0$ and $\partial_m s_U = 0$. Alternatively, we may obtain the critical excitation strength for each VSHF wavenum-

ber by setting $s_U = 0$ in (47), which gives

$$\varepsilon_c(m) = \frac{r_m}{2r} \left[\int dp dq \mathcal{F}_U \Big|_{s_U=0} \tilde{E} \right]^{-1}. \quad (55)$$

The stability boundary is then given by

$$\varepsilon_c = \min_m [\varepsilon_c(m)] = \varepsilon_c(m^*). \quad (56)$$

Figure 7 (darkest curves) shows ε_c (panel a) and the emergent VSHF wavenumber, m^* (panel b), for the case of IRE. Dashed lines provide asymptotic approximations (see Appendix D). The stability boundary reflects the properties of s_U discussed in Section 5a. When the stratification is weak, ε_c grows like $1/N_0^2$ and m^* approaches 1. This behavior reflects the small- N_0^2 structure of s_U described by (50) and shown in Figure 5. Because VSHFI develops perturbatively with increasing stratification, very weak stratification requires very strong excitation to produce an instability. As N_0^2 increases, ε_c decreases to a minimum near $N_0^2 = 10$, reflecting the peak in s_U^* near that value of N_0^2 visible in Figure 4 (a). For very strong stratification, ε_c again becomes large, growing like N_0^2 for large N_0^2 , with $m^* \rightarrow 0$. This behavior reflects the large- N_0^2 structure of s_U described by (53) and shown in Figure 6.

We compare the S3T prediction of ε_c to the behavior of the NL system in Figure 8. Because the NL system fluctuates stochastically, a precise NL stability boundary does not exist so we instead identify the onset of VSHFI with an abrupt increase of zmf, previously shown in Figure 3 (b). We carried out an NL simulation for each (ε, N_0^2) pair on the grid defined by $N_0^2 = 10^i$, $\varepsilon = 10^j$, with $i = 0, 0.5, \dots, 3$, and $j = 0, 0.5, \dots, 4$. The thick dark curve in Figure 8 shows ε_c as predicted³ by S3T and the shaded contours show the time average zmf values from the NL simulations, calculated following a spin-up period.

For intermediate and strong stratification, ε_c provides a good prediction of the onset of VSHFI in NL. In particular, the NL system verifies the S3T predictions that VSHFI occurs most readily at intermediate stratification and that the excitation strength at which VSHFI occurs grows like N_0^2 as the stratification becomes strong.

Another feature visible in Figure 8, and also in Figure 3 (b) which is a ‘slice’ through Figure 8 at $N_0^2 = 10^3$, is that the NL zmf reaches a maximum and subsequently decreases as ε is increased. This finite-amplitude effect is outside the scope of the present work, which analyzes VSHFI from a linear perspective. However, inspection of the individual simulations suggests that the eventual decrease of zmf may be due to the VSHF maintaining a relatively large vertical wavenumber as ε is increased. This behavior is in contrast to the usual observation in β -plane turbulence that jets transition to lower wavenumber

³To calculate the value of ε_c appropriate for comparison to simulations we apply (56) with m restricted to only the values permitted by the doubly periodic domain.

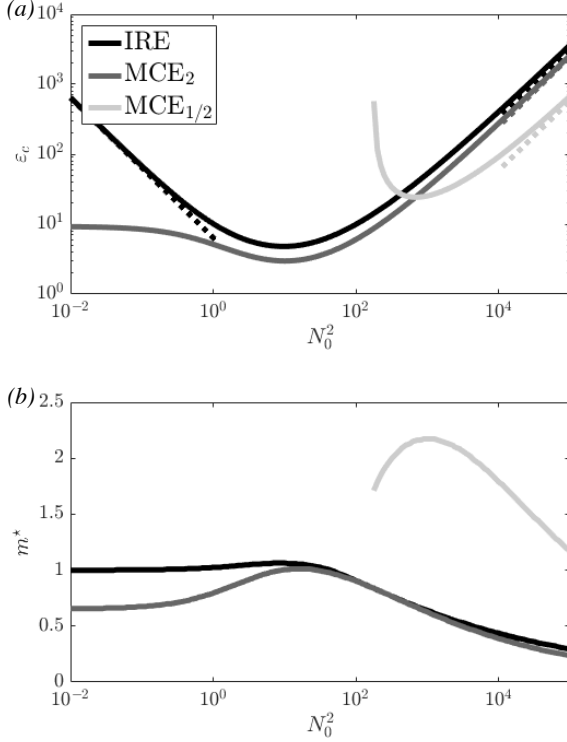


FIG. 7. Stability boundary (a) and emergent VSHF wavenumber (b) for the IRE, MCE_2 , and $MCE_{1/2}$ cases. Solid curves in (a) show the value of ϵ_c calculated using full dispersion relation and dashed lines show asymptotic approximations (see Appendices D and E). The parameters used are $r_m = 0.1$ and $\nu = 0$.

as the excitation strength is increased (Farrell and Ioannou 2007). Our previous analysis of VSHFI with matrix S3T is consistent with this interpretation, and also suggests that additional turbulent equilibria consisting of lower-wavenumber, more energetic VSHFs may be simultaneously stable with the equilibria shown in Figure 8 (Fitzgerald and Farrell 2016).

Under weak stratification ($N_0^2 \lesssim 10$), the VSHF does not obtain significant energy in our NL simulations, consistent with previous studies (Smith 2001; Kumar et al. 2017). An energetic VSHF creates strong shear, which for weak stratification is associated with hydrodynamic instability via the Miles-Howard (MH) criterion. Although the MH criterion is formally valid only for a static parallel flow in the absence of excitation and dissipation, it provides a useful guide for intuition and suggests that maintaining strong VSHFs at weak stratification is unlikely, as instability of the emergent jet is likely to prevent its obtaining significant amplitude.

b. MCE

The lighter curves in Figure 7 (a) show the stability boundaries in the MCE cases. As in the case of IRE, the

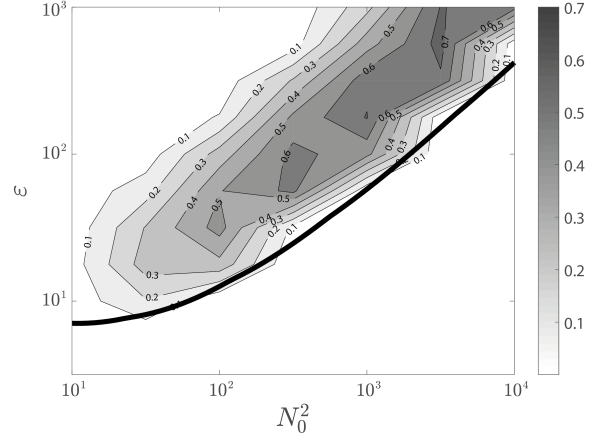


FIG. 8. Time average zmf value in NL simulations (shaded contours) compared with the VSHFI stability boundary predicted by S3T (solid curve). Turbulence is maintained with IRE and the time average zmf is calculated following a spin-up period. For intermediate and strong stratification the S3T stability boundary captures the abrupt emergence of the VSHF as ϵ is increased, including the increase of the critical excitation strength as N_0^2 is increased. The parameters used are $r_m = 0.1$ and $\nu = 0.03$.

stability boundaries reflect the properties of s_U discussed in Section 5b. Striking differences are evident between the MCE_2 and $MCE_{1/2}$ cases. As $N_0^2 \rightarrow 0$, s_U remains positive for MCE_2 and remains negative for $MCE_{1/2}$ (see Figure 4 (b,c)). As a result, for small N_0^2 , ϵ_c tends to a constant value for MCE_2 while ϵ_c does not exist for $MCE_{1/2}$ as VSHFI does not occur for any excitation strength until the stratification becomes strong. The stability boundaries also reflect the surprising result, previously shown in Figure 6, that strongly stratified homogeneous turbulence maintained with $MCE_{1/2}$ is more unstable to VSHFI than that maintained with MCE_2 or IRE, even though VSHFI does not occur at all for $MCE_{1/2}$ when the stratification is weak.

The emergent VSHF wavenumber, m^* , also differs markedly between the MCE cases (Figure 7 (b), lighter curves). For small N_0^2 , MCE_2 has $m^* \approx 0.6$ so that the vertical scale of the emergent VSHF is comparable to the horizontal scale of the excitation, $1/k_0$. When VSHFI first occurs for $MCE_{1/2}$ near $N_0^2 = 10^2$, the VSHF instead has $m^* \approx 1.6$, so that the vertical scale of the VSHF is smaller than $1/k_0$ and is associated with the correlation length of the excitation in the vertical, ℓ_c . For large N_0^2 the MCE and IRE cases all behave similarly, with $m^* \rightarrow 0$ in all cases, consistent with the results shown in Figure 6.

In the remaining sections, we revisit these observations and analyze their dynamical origins from the perspective of wave-mean flow interaction.

7. Feedback factors

Because the properties of VSHFI can depend on the choice of excitation structure, it is useful to analyze VSHFI from a perspective independent of the particular excitation. The feedback factor, first developed by Bakas et al. (2015) in the context of ZI, provides a tool for analyzing VSHFI in this way. In the feedback factor approach, the strength and sign of the feedback resulting from the interaction between the VSHF and each wavenumber component of the turbulent spectrum is analyzed independently. Each spectral component either supports or opposes VSHF development, and the total wave-mean flow feedback for a particular excitation is given by the sum of the feedbacks arising from each component. This perspective facilitates understanding the properties of VSHFI demonstrated in Section 5.

We focus on the case of a stationary, wavenumber m VSHF of perturbative amplitude at its stability boundary, so that $U = \delta U$, $\partial_t = s_U = 0$, and $\varepsilon = \varepsilon_c(m)$. From (3), the Reynolds stress and VSHF structures are related as $r_m \delta U = -\partial_z \langle u' w' \rangle$. Combining this with (55) we obtain

$$-\frac{\partial}{\partial z} \langle u' w' \rangle = \delta U \varepsilon_c(m) \iint dp dq \left(2r \mathcal{F}_U \Big|_{s_U=0} \right) \tilde{E}. \quad (57)$$

The induced Reynolds stress in (57) scales linearly with δU , which follows from linearization, and also with ε , which follows from the quasilinearity of the dynamics underlying S3T. The remaining factor in (57), which determines the sign of the induced stress, is the integral over the excitation spectrum, \tilde{E} , weighted by the feedback factor for each spectral component, $2r \mathcal{F}_U$, evaluated at $s_U = 0$. We hereafter refer to \mathcal{F}_U as the feedback factor for simplicity, as the $2r$ factor scales the amplitude but does not modify the structure, and suppress the notation indicating that \mathcal{F}_U is evaluated at $s_U = 0$.

The feedback factor depends on the four arguments (p, q, N_0^2, m) and characterizes the wave-mean flow feedback occurring between waves excited with wavenumber (p, q) and a weak VSHF with wavenumber m . If the net feedback is positive when integrated over the excited spectrum in (57), the induced Reynolds stress divergence is proportional to δU and reinforces the VSHF so that VSHFs at wavenumber m grow for sufficiently large ε . If the net feedback is negative, the Reynolds stress divergence opposes the VSHF and VSHFs at wavenumber m decay faster than r_m . The feedback factor thus underlies VSHFI and understanding the structure of \mathcal{F}_U is central for understanding VSHFI.

The complete structure of \mathcal{F}_U cannot be visualized at once due to its many arguments. However, when the excitation structure is particularly simple, such as IRE and MCE which excite 1D subspaces of the available 2D spectrum, the relevant \mathcal{F}_U structure can be visualized easily.

Figure 9 shows the \mathcal{F}_U structure relevant to IRE in polar coordinates, with the radial coordinate indicating m and the polar angle indicating the angle of the excited wave, θ , where $(p, q) = (\cos \theta, \sin \theta)$. As IRE is doubly mirror-symmetric, with $\tilde{E}(p, q) = \tilde{E}(-p, q) = \tilde{E}(p, -q) = \tilde{E}(-p, -q)$, we sum the contributions to \mathcal{F}_U from each of these related Fourier components and plot the resulting \mathcal{F}_U values over the first quadrant, $0 \leq \theta \leq \pi/2$. Red regions in Figure 9 correspond to $\mathcal{F}_U > 0$ and produce Reynolds stresses that reinforce the VSHF, while blue regions correspond to the opposite case, $\mathcal{F}_U < 0$. The net wave-mean flow interaction between the IRE spectrum and a VSHF with wavenumber m_0 is determined by comparing the size and strength of the $\mathcal{F}_U > 0$ and $\mathcal{F}_U < 0$ regions over the contour $m = m_0$.

We showed in Figure 5 that unstratified IRE turbulence has no net influence on VSHFs with $0 < m < 1$, so that $s_U = -r_m$, and that turbulence opposes VSHFs with $m > 1$, so that $s_U < -r_m$. Figure 9 (a) provides an explanation for this behavior. VSHFs with $0 < m < 1$ are supported by waves with small θ and opposed by waves with larger θ . These competing effects cancel exactly, resulting in zero net feedback. For $m > 1$ the range of θ for which $\mathcal{F}_U < 0$ widens, resulting in negative net feedback.

We also showed in Figure 5 that for weak but nonzero stratification, s_U is enhanced for $0 < m < 1$ relative to the $N_0^2 = 0$ case, with the strongest enhancement at $m = 1$. The changes in \mathcal{F}_U as N_0^2 is increased from zero, shown in Figure 9 (b), explain this observation. The symmetry between the $\mathcal{F}_U > 0$ and $\mathcal{F}_U < 0$ regions for $0 < m < 1$ is broken when $N_0^2 > 0$, favoring $\mathcal{F}_U > 0$ for most (m, θ) pairs but especially near $m \approx 1$ for small θ . S3T thus predicts that an $m = 1$ VSHF emerges in weakly stratified IRE turbulence near the stability boundary.

Figure 7 showed that VSHFI occurs for MCE₂ when $N_0^2 = 0$ but does not occur for MCE_{1/2} until the stratification is strong. Figure 10 shows the \mathcal{F}_U structure that underlies this behavior, now using Cartesian coordinates appropriate for the MCE in which the horizontal axis indicates the VSHF wavenumber, m , and the vertical axis indicates the vertical wavenumber of the excited wave, q . As in the case of IRE, we sum the contributions to \mathcal{F}_U from Fourier components that are related by the double mirror symmetry of MCE and plot the result over $q > 0$. For reference, Figure 12 (a) shows the 1D energy injection spectra, $\tilde{E}(q)$, for MCE₂ and MCE_{1/2}. MCE₂ primarily excites $q \lesssim 1$ while MCE_{1/2} injects significant energy over $q \lesssim 4$. The $\mathcal{F}_U(N_0^2 = 0)$ structure in Figure 10 (a) shows that the $q < 1$ region excited by MCE₂ predominantly has $\mathcal{F}_U > 0$ for $m < 1$, explaining the occurrence of VSHFI for unstratified MCE₂ with $m^* \approx 0.6$. Although MCE_{1/2} excites the same $q < 1$ waves, it also excites a broad band of $q > 1$ waves with $\mathcal{F}_U < 0$, resulting in $s_U < 0$ for $N_0^2 = 0$.

In Section 6 we discussed the surprising result that, under strong stratification, VSHFI occurs at lower ε for

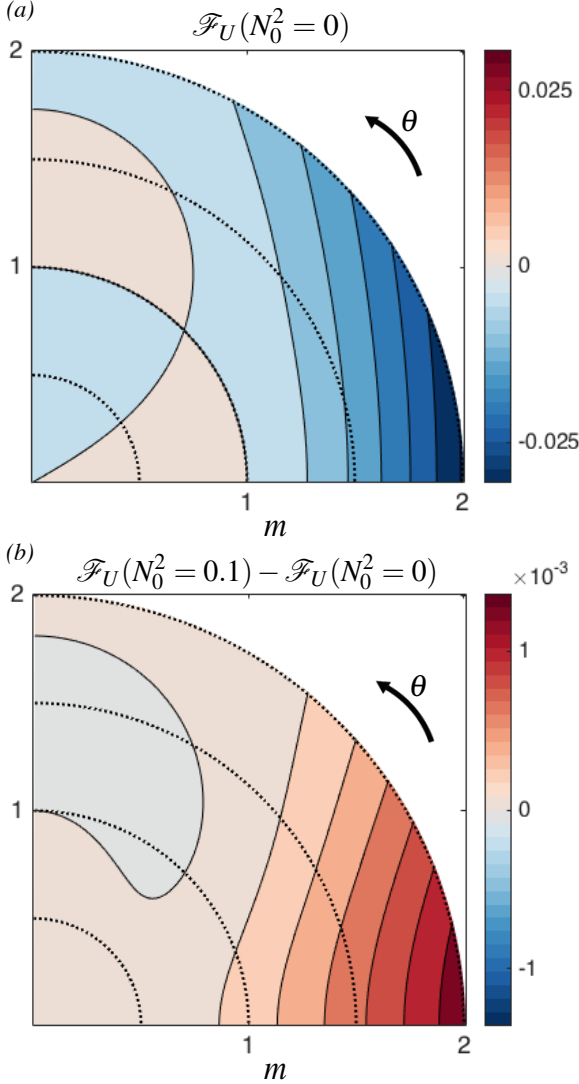


FIG. 9. VSHFI wave-mean flow feedback factor, \mathcal{F}_U , for the cases of zero and weak stratification, shown in polar coordinates appropriate for analyzing IRE. The radial coordinate indicates the VSHF wavenumber, m , and the polar angle indicates the angle of the excited wave according with the convention $(p, q) = (\cos \theta, \sin \theta)$. Panel (a) shows \mathcal{F}_U for $N_0^2 = 0$ and panel (b) shows how \mathcal{F}_U is modified by the introduction of weak stratification. The parameters used are $r_m = 0.1$ and $\nu = 0$.

$\text{MCE}_{1/2}$ than for MCE_2 (Figure 7 (a)). The structure of \mathcal{F}_U for large N_0^2 , shown in Figure 10 (b), explains this phenomenon. For large N_0^2 , a broad band of $\mathcal{F}_U > 0$ waves exists for $q > 1$. This band is excited by $\text{MCE}_{1/2}$, leading to strong VSHFI for large N_0^2 . The $q < 1$ band excited by MCE_2 exhibits a dipole structure in which waves that strongly reinforce the VSHF compete with others that strongly oppose it, weakening the net feedback and the VSHFI growth rate for MCE_2 .

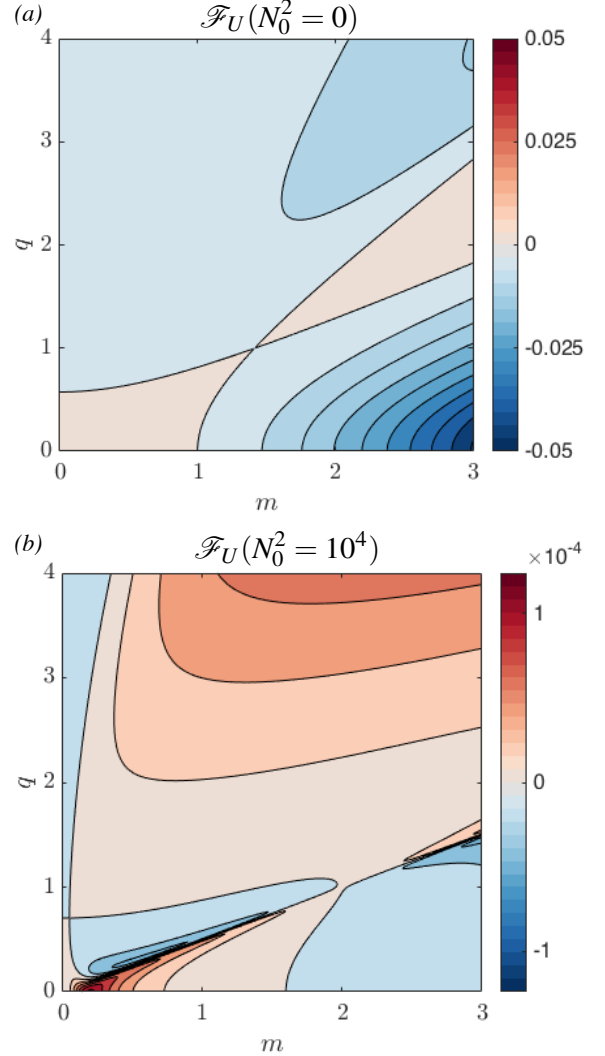


FIG. 10. VSHFI feedback factor, \mathcal{F}_U , in Cartesian coordinates appropriate for analyzing MCE. The horizontal axis indicates the VSHF wavenumber, m , and the vertical axis indicates the vertical wavenumber of the excited wave, q . Panel (a) shows \mathcal{F}_U in the unstratified case ($N_0^2 = 0$) and panel (b) shows \mathcal{F}_U under strong stratification ($N_0^2 = 10^4$). The parameters used are $r_m = 0.1$ and $\nu = 0$.

Feedback factor analysis can also be applied to HMBLI. Following the approach for VSHFI, the feedback factor $\mathcal{F}_B(p, q, N_0^2, m)$ characterizes the feedback between waves excited at wavenumber (p, q) and weak HMBLs with wavenumber m . The structure of \mathcal{F}_B is shown in Figure 11, revealing that the feedback is usually negative, with a narrow band of positive interactions emerging at strong stratification. As a result, HMBLI fails to occur for either IRE or MCE, which do not preferentially excite the $\mathcal{F}_B > 0$ band available at strong stratification.

The existence of an $\mathcal{F}_B > 0$ band in Figure 11 (b) raises the intriguing possibility that preferential excitation of this band might produce turbulence in which HMBLI occurs.

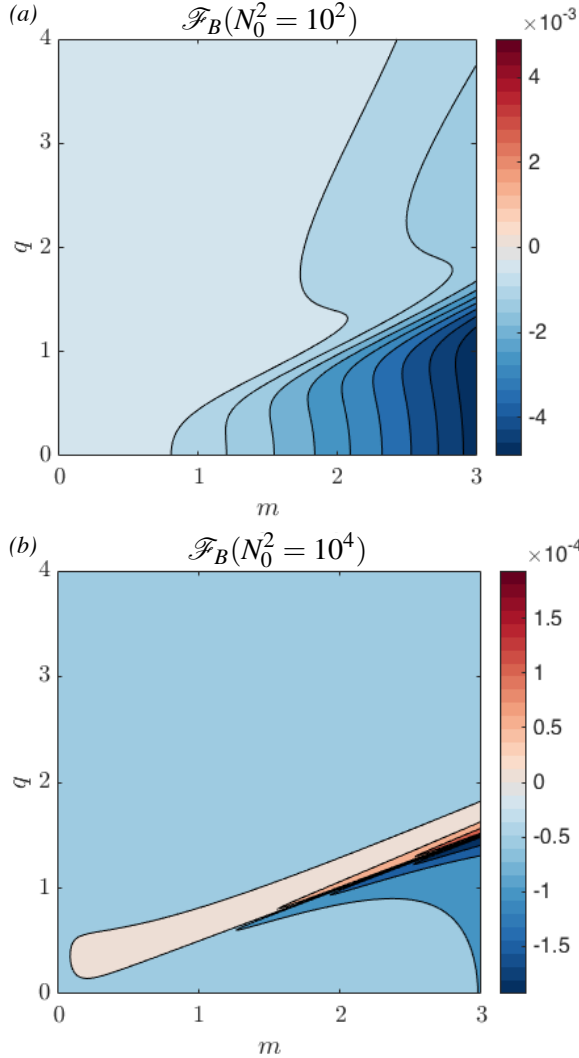


FIG. 11. HMBLI feedback factor, \mathcal{F}_B , in Cartesian coordinates as in Figure 10. Panel (a) shows \mathcal{F}_B under intermediate stratification ($N_0^2 = 10^2$) and panel (b) shows \mathcal{F}_B under strong stratification ($N_0^2 = 10^4$). This figure shows that the feedback is usually negative, consistent with the observation that HMBLI does not occur for IRE or MCE. However, panel (b) shows that a band of positive feedback exists in the strongly stratified case. The parameters used are $r_m = 0.1$ and $\nu = 0$.

In Figure 12 we demonstrate that HMBLI indeed occurs with a faster growth rate than VSHFI when the excitation is carefully chosen. Panel (a) shows the chosen excitation, which is highly localized near $q = 1$. Waves excited with $q \approx 1$ engage in a strong positive feedback with $m \approx 2$ HMBLs. Although these waves also engage in a positive feedback with $m \lesssim 1$ VSHFs, the net HMBLI feedback is stronger than the net VSHFI feedback. Panel (b) shows s_U and s_B as functions of m for the localized excitation. As anticipated from feedback factor analysis, the fastest growing coherent structures are HMBLs with $m \approx 1.8$, and $s_U < 0$ for all m . It is thus possible for density lay-

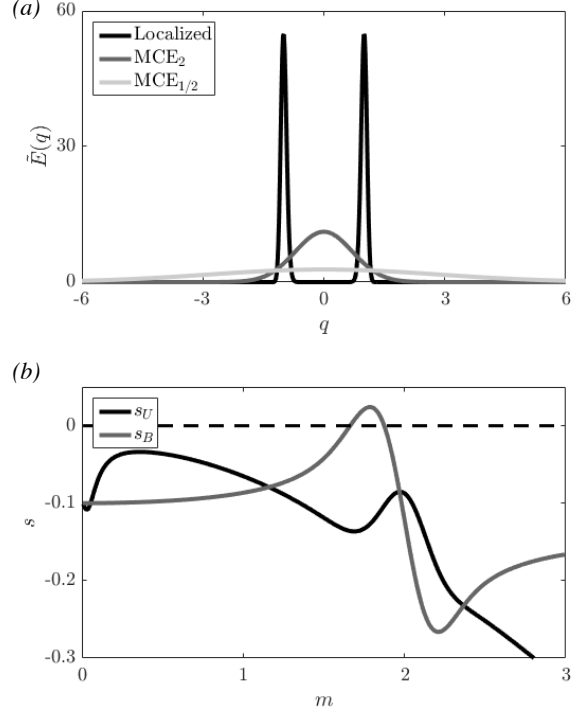


FIG. 12. Example demonstrating that HMBLI can occur for appropriately chosen excitation. Panel (a) shows the energy injection spectrum for the localized excitation chosen to induce HMBLI alongside the MCE₂ and MCE_{1/2} spectra which are provided for reference. Panel (b) shows the VSHFI and HMBLI growth rates as functions of m for the localized excitation with parameters $\varepsilon = 400$ and $N_0^2 = 10^4$. The most unstable structure corresponds to HMBLs with $m \approx 1.8$, which emerge from homogeneous turbulence as an S3T instability. The parameters used are $r_m = 0.1$ and $\nu = 0$.

ers to spontaneously form in homogeneous turbulence via quasilinear interactions between the emergent layers and the wave field. However, because the turbulent spectrum required for this scenario is highly contrived, this mechanism is unlikely to be found in nature or in numerical simulations using more natural excitation.

8. Processes Contributing to Wave-Mean Flow Feedback

The quasilinear wave-mean flow feedback mechanism characterized by \mathcal{F}_U operates via several physical processes. One such process, sometimes referred to as the Orr mechanism, is shear straining of vorticity perturbations by the VSHF to produce upgradient momentum fluxes. We now briefly analyze the contributions of individual processes to VSHFI. This analysis reveals that different processes can act as the dominant driver of VSHFI for different choices of excitation.

The Reynolds stresses that reinforce the VSHF during its exponential growth phase are associated, through (29), with perturbations to the vorticity covariance, δZ . Three

quasilinear processes, represented by terms in (43), produce structure in δZ that yields Reynolds stresses. The first process, represented by the term $(\delta U_1 - \delta U_2)\partial_x Z_H$, is the previously described Orr mechanism. The second process, represented by the term $-(\delta U_1'' - \delta U_2'')\Delta\partial_x \Psi_H$, is the advection of the VSHF vorticity by the perturbations. The third process, represented by the term $-\partial_x(\delta\Gamma^b - \delta\Gamma^c)$, is the production of vorticity perturbations by buoyancy perturbations. The third process is the most complex as it subsumes a variety of processes involving vorticity-buoyancy coupling such as gravity wave dynamics. The feedback factor, \mathcal{F}_U , can be decomposed into contributions from each of these processes as

$$\mathcal{F}_U = \mathcal{F}_U^{Orr} + \mathcal{F}_U^{cu} + \mathcal{F}_U^{wave}, \quad (58)$$

where the superscripts identify the component feedbacks resulting from the Orr mechanism (Orr), from advection of VSHF vorticity by perturbations (cu, for curvature), and from vorticity-buoyancy coupling including gravity wave dynamics (wave). Mathematical details are provided in Appendix F. We note that only \mathcal{F}_U^{wave} depends on the stratification, N_0^2 , as the Orr and curvature feedbacks do not involve vorticity-buoyancy coupling.

To illustrate this technique we apply (58) to VSHFI in the case of MCE. Figure 13 shows the contribution of each process to \mathcal{F}_U for $N_0^2 = 10^4$. In Section 6 we showed that MCE₂, which primarily excites waves with $q < 1$, forms a VSHF with $m \approx 0.5$ for these parameter values, while MCE_{1/2}, which excites waves with $q \lesssim 4$, forms a VSHF with $m \approx 1.5$. Inspection of the region $m \approx 0.5$, $0 < q < 1$ in Figure 13 indicates that VSHFI for MCE₂ is driven by the Orr mechanism, and that the curvature and wave feedbacks oppose VSHFI. In contrast, the region $m \approx 1.5$, $q \lesssim 4$ in Figure 13 indicates that VSHFI for MCE_{1/2} is driven by the wave feedback. The net feedbacks from Orr and curvature dynamics result from a competition between negative and positive feedbacks from different parts of the spectrum, and detailed integration reveals that both processes oppose VSHFI. The quasilinear feedback mechanism thus produces VSHFI for both MCE₂ and MCE_{1/2} but leverages distinct physical processes in each case.

9. Discussion

In this work we applied S3T to analyze VSHF formation in 2D stratified turbulence. We focused on the initial VSHF emergence in homogeneous turbulence maintained by stochastic excitation. VSHF emergence occurs through an S3T instability of homogeneous turbulence which we refer to as VSHFI. Some properties of VSHFI, such as the shape of the stability boundary, the scale of the emergent VSHF, and the detailed physical mechanism of VSHFI depend on the structure of the stochastic excitation. We explained these properties in terms of the statistical wave-mean flow feedback mechanism which drives VSHFI and

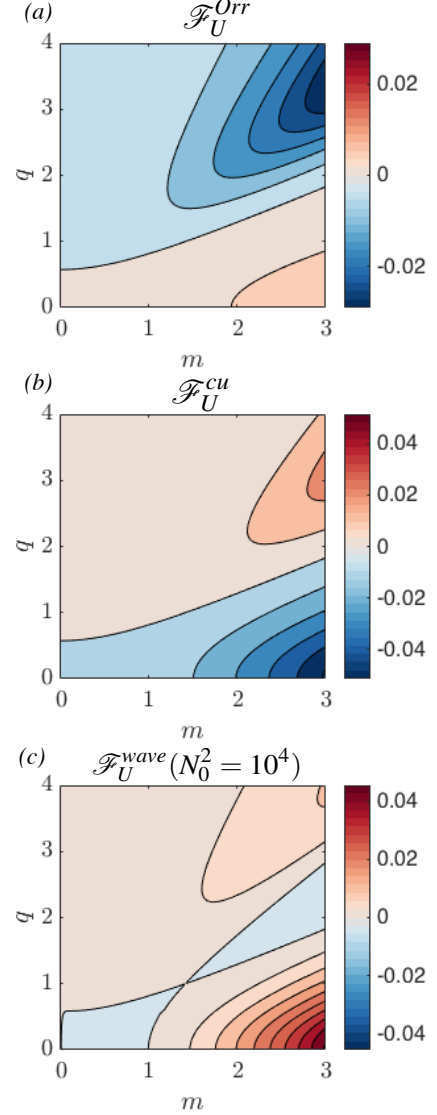


FIG. 13. Decomposition of the VSHFI feedback factor, \mathcal{F}_U , into its contributions from the Orr (a), curvature (b), and wave (c) feedbacks as in (58). Axes are as in Figure 10. The Orr and curvature feedbacks are independent of N_0^2 and the wave feedback is shown under strong stratification ($N_0^2 = 10^4$). This decomposition shows that the $m \approx 0.5$ VSHF emerging for MCE₂, which primarily excites $q \lesssim 1$, is primarily driven by the Orr mechanism, while the $m \approx 1.5$ VSHF emerging for MCE_{1/2}, which excites $q \lesssim 4$, is primarily driven by vorticity-buoyancy coupling. The parameters used are $r_m = 0.1$ and $\nu = 0$.

the basic physical processes that underlie the feedback. Our analysis complements recent work in which we applied S3T to analyze VSHFs at finite amplitude (Fitzgerald and Farrell 2016).

Our analysis extended to VSHFI several S3T concepts and techniques developed in the context of ZI in β -plane turbulence. In particular, a primary contribution of this work was to extend to VSHFI the closed-form linearized

formulation of S3T due to SY12. The SY12 approach to S3T is invaluable for understanding the initial emergence of coherent structure in turbulence because it allows the parameter dependence and asymptotic behavior to be analyzed using closed-form expressions. We emphasize, however that this approach is formally equivalent to the conventional matrix implementation of S3T described in Appendix A. St-Onge and Krommes (2017) recently extended the SY12 approach to the turbulence of stochastically excited interchange modes in plasmas. This turbulence is equivalent to stochastically excited Rayleigh-Bénard convection for subcritical Rayleigh number, which is a weakly unstably stratified turbulence closely related to the stably stratified turbulence that we analyze.

VSHFI is revealed by our analysis to be similar to ZI in several respects. Comparison of VSHFI and ZI reveals that the role played by the stratification, N_0^2 , in VSHFI is instead played by the planetary vorticity gradient, β , in ZI. For example, for IRE turbulence the ZI growth rate decays like $1/\beta^2$ as $\beta \rightarrow \infty$ and increases from zero like β^2 for small β in the absence of explicit jet damping. Bakas et al. (2015) also showed that the properties of ZI depend on the structure of the stochastic excitation. In particular, structures that primarily excite Rossby waves with nearly horizontal wavevectors produce positive ZI growth rates as $\beta \rightarrow 0$, whereas ZI does not occur at all for weak β for structures that primarily excite waves with nearly vertical wavevectors. These properties mirror the properties of VSHFI analyzed in this paper. From the S3T perspective, zonal jet emergence in geostrophic turbulence and VSHF emergence in non-rotating stratified turbulence can be usefully conceptualized as two instances of the more generic phenomenon of S3T instability of homogeneous turbulence.

Acknowledgments. The authors thank N. C. Constantinou for helpful discussions and J. R. Taylor for providing the DIABLO code. J. G. F. was partially supported by a doctoral fellowship from the National Sciences and Engineering Research Council of Canada. B. F. F. was partially

supported by the U.S. National Science Foundation under Grant Nos. NSF AGS-1246929 and NSF AGS-1640989.

APPENDIX A

S3T Dynamics in Matrix Form

In this Appendix we provide a brief derivation of the S3T equations of motion in matrix form. Our presentation is based on Fitzgerald and Farrell (2016), in which additional details can be found. As the dynamics underlying S3T are QL, we begin with the QL equations of motion which are comprised of the perturbation equations (17)-(18) together with the mean equations (3)-(4). Addressing first the perturbation dynamics, we expand the perturbation streamfunction and buoyancy fields in Fourier series in horizontal wavenumber as

$$\psi'(x, z, t) = \text{Re} \left[\sum_{n=1}^{N_p} \tilde{\psi}_n(z, t) e^{ip_n x} \right], \quad (\text{A1})$$

$$b'(x, z, t) = \text{Re} \left[\sum_{n=1}^{N_p} \tilde{b}_n(z, t) e^{ip_n x} \right], \quad (\text{A2})$$

where N_p is the number Fourier modes retained in the calculation and $p_n = 2\pi n/L$, where L is the horizontal extent of the domain. In a discretized numerical system the mean fields, U and B , and the perturbation Fourier coefficients, $\tilde{\psi}_n$ and \tilde{b}_n , correspond to vectors. The equations of motion for $\tilde{\psi}_n$ and \tilde{b}_n can be written in the matrix-vector form

$$\frac{d}{dt} \begin{pmatrix} \tilde{\psi}_n \\ \tilde{b}_n \end{pmatrix} = \mathbb{A}_n(\vec{U}, \vec{B}) \begin{pmatrix} \tilde{\psi}_n \\ \tilde{b}_n \end{pmatrix} + \sqrt{\varepsilon} \begin{pmatrix} \tilde{\xi}_n^\psi \\ \tilde{\xi}_n^b \end{pmatrix}. \quad (\text{A3})$$

in which $\tilde{\xi}_n^\psi$ and $\tilde{\xi}_n^b$ are the vector Fourier coefficients of the stochastic excitation of the perturbation streamfunction and buoyancy fields, and \mathbb{A}_n is the linear matrix operator

$$\mathbb{A}_n = \begin{pmatrix} -ip_n \mathbb{L}_n^{-1} \text{diag}(\vec{U}) \mathbb{L}_n + ip_n \mathbb{L}_n^{-1} \text{diag}(\mathbb{D}^2 \vec{U}) - r\mathbb{I} + v\mathbb{L}_n & ip_n \mathbb{L}_n^{-1} \\ -ip_n N_0^2 \mathbb{I} - ip_n \text{diag}(\mathbb{D} \vec{B}) & -ip_n \text{diag}(\vec{U}) - r\mathbb{I} + v\mathbb{L}_n \end{pmatrix}. \quad (\text{A4})$$

Here \mathbb{D} is the discretized vertical derivative operator, \mathbb{I} is the identity matrix, $\mathbb{L}_n \equiv \mathbb{D}^2 - p_n^2 \mathbb{I}$ is the discretized Laplacian at wavenumber p_n , and $\text{diag}(\vec{V})$ denotes the diagonal matrix for which the nonzero elements are given by the entries of the column vector \vec{V} .

To obtain the S3T closure we apply the ergodic assumption that horizontal averages and ensemble averages are equal. Under this assumption, the perturbation covariance

matrix, defined as

$$\mathbb{C}_n = \begin{pmatrix} \langle \tilde{\psi}_n \tilde{\psi}_n^\dagger \rangle & \langle \tilde{\psi}_n \tilde{b}_n^\dagger \rangle \\ \langle \tilde{b}_n \tilde{\psi}_n^\dagger \rangle & \langle \tilde{b}_n \tilde{b}_n^\dagger \rangle \end{pmatrix} = \begin{pmatrix} \mathbb{C}_{\psi\psi,n} & \mathbb{C}_{\psi b,n} \\ \mathbb{C}_{b\psi,n}^\dagger & \mathbb{C}_{bb,n} \end{pmatrix}, \quad (\text{A5})$$

obeys the time-dependent Lyapunov equation

$$\frac{d}{dt} \mathbb{C}_n = \mathbb{A}_n(\vec{U}, \vec{B}) \mathbb{C}_n + \mathbb{C}_n \mathbb{A}_n(\vec{U}, \vec{B})^\dagger + \varepsilon \mathbb{Q}_n, \quad (\text{A6})$$

in which daggers indicate Hermitian conjugation and \mathbb{Q}_n is the covariance matrix of the stochastic excitation, defined as

$$\mathbb{Q}_n = \begin{pmatrix} \langle \vec{\xi}_n^\psi \vec{\xi}_n^\psi, \dagger \rangle & \langle \vec{\xi}_n^\psi \vec{\xi}_n^{b, \dagger} \rangle \\ \langle \vec{\xi}_n^b \vec{\xi}_n^\psi, \dagger \rangle & \langle \vec{\xi}_n^b \vec{\xi}_n^{b, \dagger} \rangle \end{pmatrix}. \quad (\text{A7})$$

The divergence of the ensemble mean Reynolds stress and of the ensemble mean eddy buoyancy flux can be written in terms of the perturbation covariance matrix as

$$-\frac{\partial}{\partial z} \langle u'w' \rangle = \sum_{n=1}^{N_p} \frac{p_n}{2} \text{Im} [\text{vecd}(\mathbb{L}_n \mathbb{C}_{\psi\psi, n})], \quad (\text{A8})$$

$$-\frac{\partial}{\partial z} \langle w'b' \rangle = \sum_{n=1}^{N_p} \frac{p_n}{2} \text{Im} [\text{vecd}(\mathbb{D} \mathbb{C}_{\psi b, n})], \quad (\text{A9})$$

in which $\text{vecd}(\mathbb{M})$ denotes the vector comprised of the diagonal elements of the matrix \mathbb{M} . The dynamics of \vec{U} and \vec{B} can then be written as

$$\frac{d}{dt} \vec{U} = \sum_{n=1}^{N_p} \frac{p_n}{2} \text{Im} [\text{vecd}(\mathbb{L}_n \mathbb{C}_{\psi\psi, n})] - r_m \vec{U} + \nu \mathbb{D}^2 \vec{U}, \quad (\text{A10})$$

$$\frac{d}{dt} \vec{B} = \sum_{n=1}^{N_p} \frac{p_n}{2} \text{Im} [\text{vecd}(\mathbb{D} \mathbb{C}_{\psi b, n})] - r_m \vec{B} + \nu \mathbb{D}^2 \vec{B}. \quad (\text{A11})$$

Equations (A6), (A10), and (A11) together constitute the matrix form of the S3T dynamics.

To obtain the S3T results shown in Figure 3, the S3T dynamics was integrated numerically to equilibrium using a fourth-order Runge-Kutta method with 64 grid points in the vertical direction and $N_p = 8$. The covariance matrix of the excitation, \mathbb{Q} , was chosen to match the ring excitation used in our NL and QL simulations. To initialize the system the perturbation covariance matrix, \mathbb{C} , was set to the matrix corresponding to the homogeneous turbulence fixed point given by (42). The mean fields, \vec{U} and \vec{B} , were initialized as small random perturbations.

APPENDIX B

S3T Dynamics in Continuous Form

In this Appendix we provide additional details regarding the derivation of the S3T equations of motion in continuous form, (26)-(31). We illustrate the derivation of the S3T perturbation covariance equations of motion, (26)-(28), using the equation of motion for the vorticity covariance, Z . The QL perturbation vorticity equation (17) at an arbitrary point \vec{x}_i may be written as

$$\partial_t \zeta_i' = \mathcal{D}_i + \sqrt{\varepsilon} \xi_i^\zeta, \quad (\text{B1})$$

where \mathcal{D}_i represents the deterministic dynamics and is given by

$$\mathcal{D}_i = -U_i \partial_{x,i} \zeta_i' + U_{z,i} \partial_{x,i} \psi_i' + \partial_{x,i} b_i' - (r - \nu \Delta_i) \zeta_i'. \quad (\text{B2})$$

The equation of motion for the product $\zeta_1' \zeta_2'$ is given by Itô's formula as

$$\partial_t \zeta_1' \zeta_2' = \zeta_1' \mathcal{D}_2 + \zeta_2' \mathcal{D}_1 + \varepsilon \Xi + \zeta_1' \xi_2^\zeta + \zeta_2' \xi_1^\zeta. \quad (\text{B3})$$

To form the equation of motion for $Z \equiv \langle \zeta_1' \zeta_2' \rangle$ we take the ensemble average of (B3). Upon ensemble averaging the stochastic terms vanish as the excitation is uncorrelated with the system state and we obtain

$$\begin{aligned} \partial_t Z = & -(U_1 - U_2) \partial_x Z + (U_1'' \Delta_2 - U_2'' \Delta_1) \partial_x \Psi \\ & + \partial_x (\Gamma^b - \Gamma^\zeta) - 2[r - \frac{1}{2} \nu (\Delta_1 + \Delta_2)] Z + \varepsilon \Xi, \end{aligned} \quad (\text{B4})$$

in which we have made use of the collective coordinate $x = x_1 - x_2$ and the corresponding derivative relations $\partial_{x,1} = \partial_x$ and $\partial_{x,2} = -\partial_x$. Note that we have set $\partial_{\bar{x}} = 0$, where $\bar{x} = \frac{1}{2}(x_1 + x_2)$, due to the assumed horizontal statistical symmetry of the system.

To obtain (26) we make use of the additional collective coordinates $z = z_1 - z_2$ and $\bar{z} = \frac{1}{2}(z_1 + z_2)$. In these coordinates the operators $\partial_{z,i}$ and Δ_i are written as

$$\partial_{z,i} = (-1)^{1+i} \partial_z + \frac{1}{2} \partial_{\bar{z}}, \quad \Delta_i = \Delta - (-1)^i \partial_{z\bar{z}}^2 + \frac{1}{4} \partial_{\bar{z}\bar{z}}^2, \quad (\text{B5})$$

in which Δ is the Laplacian in the difference variables, $\Delta = \partial_{xx}^2 + \partial_{zz}^2$. When obtaining (26), a useful simplifying result is $U_1'' \Delta_2 - U_2'' \Delta_1 = (U_1'' - U_2'')(\Delta + \frac{1}{4} \partial_{\bar{z}}^2) - (U_1'' + U_2'') \partial_{z\bar{z}}^2$.

To obtain equations (30)-(31) for the mean fields, U and B , it is necessary to write the perturbation fluxes $\langle u'w' \rangle$ and $\langle w'b' \rangle$ in terms of the perturbation covariances as in (29). We illustrate the derivation using the eddy momentum flux. The eddy momentum flux may be written as

$$\langle u'w' \rangle(\bar{z}) = \frac{1}{2} (\langle u_1' w_2' \rangle + \langle u_2' w_1' \rangle) \Big|_{x=z=0}, \quad (\text{B6})$$

in which we have written the eddy flux at a level \bar{z} in terms of the two-point covariance of the perturbation velocities evaluated in the case in which \vec{x}_1 and \vec{x}_2 coincide so that $x = z = 0$ in collective coordinates. Re-writing (B6) in terms of the streamfunction covariance, Ψ , we have

$$\langle u'w' \rangle \Big|_{\bar{z}} = -(\partial_{z,1} \partial_{x,2} + \partial_{z,2} \partial_{x,1}) \Psi \Big|_{x=z=0}, \quad (\text{B7})$$

which gives (29) after transforming derivatives into collective coordinates using (B5).

APPENDIX C

VSHFI and HMBLI Dispersion Relations

In this Appendix we provide additional details regarding the derivation of equations (47) and (48) for the growth rates of VSHFI and HMBLI.

Linearizing (26)-(28) about the fixed point corresponding to homogeneous turbulence given by (42), we obtain

$$\begin{aligned} \partial_t \delta Z + (\delta U_1 - \delta U_2) \partial_x Z_H - (\delta U_1'' - \delta U_2'') \Delta \partial_x \Psi_H \\ = -2[r - v(\Delta + \frac{1}{4} \partial_{zz}^2)] \delta Z + \partial_x \delta \Gamma^{\text{diff}}, \end{aligned} \quad (\text{C1})$$

$$\begin{aligned} \partial_t \delta T + (\delta U_1 - \delta U_2) \partial_x T_H - N_0^2 \partial_x \delta S^{\text{diff}} = \\ -2[r - v(\Delta + \frac{1}{4} \partial_{zz}^2)] \delta T, \end{aligned} \quad (\text{C2})$$

$$\begin{aligned} \partial_t \delta \Gamma^{\text{sum}} - 2N_0^2 \partial_{xz}^3 \delta \Psi + (\delta B_1' - \delta B_2') \Delta \partial_x \Psi_H = \\ -2[r - v(\Delta + \frac{1}{4} \partial_{zz}^2)] \delta \Gamma^{\text{sum}}, \end{aligned} \quad (\text{C3})$$

$$\begin{aligned} \partial_t \Gamma^{\text{diff}} + 2N_0^2 (\Delta + \frac{1}{4} \partial_{zz}^2) \partial_x \delta \Psi + (\delta B_1' + \delta B_2') \Delta \partial_x \Psi_H \\ = -2[r - v(\Delta + \frac{1}{4} \partial_{zz}^2)] \delta \Gamma^{\text{diff}} - 2 \partial_x \delta T, \end{aligned} \quad (\text{C4})$$

$$\partial_t \delta U = (-r_m + v \partial_{zz}^2) \delta U - \partial_{xz}^3 \delta \Psi \Big|_{x=z=0}, \quad (\text{C5})$$

$$\partial_t \delta B = (-r_m + v \partial_{zz}^2) \delta B + \frac{1}{2} \partial_{xz}^2 \delta S^{\text{diff}} \Big|_{x=z=0}. \quad (\text{C6})$$

In these equations, for convenience, we have expressed the dynamics in terms of the quantities

$$\Gamma^{\text{sum}} \equiv \Gamma^b + \Gamma^\zeta, \quad \Gamma^{\text{diff}} \equiv \Gamma^b - \Gamma^\zeta, \quad (\text{C7})$$

$$S^{\text{sum}} \equiv S^b + S^\zeta, \quad S^{\text{diff}} \equiv S^b - S^\zeta, \quad (\text{C8})$$

which are related through the expressions

$$\Gamma^{\text{sum}} = (\Delta + \frac{1}{4} \partial_{zz}^2) S^{\text{sum}} - \partial_{zz}^2 S^{\text{diff}}, \quad (\text{C9})$$

$$\Gamma^{\text{diff}} = (\Delta + \frac{1}{4} \partial_{zz}^2) S^{\text{diff}} - \partial_{zz}^2 S^{\text{sum}}. \quad (\text{C10})$$

We analyze the linearized system (C1)-(C6) in Fourier space, using the ansatz (44)-(46) and further writing $\hat{C}_{m,s}(x, z)$, the homogeneous structure of the perturbation to the covariance function, using its Fourier transform

$$\hat{C}_{m,s}(x, z) = \iint \frac{dp dq}{(2\pi)^2} e^{i(px+qz)} \tilde{C}(p, q)_{m,s}. \quad (\text{C11})$$

Using the relations

$$\delta U_1 - \delta U_2 = 2i \sin(mz/2) e^{im\bar{z}} e^{st} \hat{U}_{m,s}, \quad (\text{C12})$$

$$\delta U_1'' - \delta U_2'' = -2im^2 \sin(mz/2) e^{im\bar{z}} e^{st} \hat{U}_{m,s}, \quad (\text{C13})$$

$$\delta B_1' - \delta B_2' = -2m \sin(mz/2) e^{im\bar{z}} e^{st} \hat{B}_{m,s}, \quad (\text{C14})$$

$$\delta B_1' + \delta B_2' = 2im \cos(mz/2) e^{im\bar{z}} e^{st} \hat{B}_{m,s}, \quad (\text{C15})$$

we obtain the linearized dynamics in Fourier space as

$$0 = s' \tilde{Z} - ip \hat{U} (\tilde{\Phi}_H^+ - \tilde{\Phi}_H^-) - ip \tilde{\Gamma}^{\text{diff}} \quad (\text{C16})$$

$$0 = s' \tilde{T} - ip \hat{U} (\tilde{T}_H^+ - \tilde{T}_H^-) - ip N_0^2 \tilde{S}^{\text{diff}} \quad (\text{C17})$$

$$0 = s' \tilde{\Gamma}^{\text{sum}} + 2impq N_0^2 \tilde{\Psi} + mp \hat{B} (\tilde{X}_H^+ - \tilde{X}_H^-) \quad (\text{C18})$$

$$0 = s' \tilde{\Gamma}^{\text{diff}} - 2ip N_0^2 (h^2 + \frac{m^2}{4}) \tilde{\Psi} - mp \hat{B} (\tilde{X}_H^- + \tilde{X}_H^+) + 2ip \tilde{T} \quad (\text{C19})$$

$$\bar{s} \hat{U} = im \iint \frac{dp dq}{(2\pi)^2} p q \tilde{\Psi} \quad (\text{C20})$$

$$\bar{s} \hat{B} = -\frac{m}{2} \iint \frac{dp dq}{(2\pi)^2} p \tilde{S}^{\text{diff}} \quad (\text{C21})$$

where we have suppressed the m, s subscripts, defined the quantities $s' = s + 2(r + v(h^2 + m^2/4))$, $\bar{s} = s + r_m + vm^2$, $\Phi_H = (\Delta^2 + m^2 \Delta) \Psi_H$, and $X_H = \Delta \Psi_H$, and introduced the notation $\tilde{f}^\pm = \tilde{f}(p, q \pm \frac{m}{2})$.

We now manipulate (C16)-(C21) to obtain the VSHFI and HMBLI dispersion relations. The dispersion relations for each instability can be obtained separately because the eigenproblem defined by (C16)-(C21) factors into two decoupled eigenproblems, one for VSHFI and one for HMBLI, under the assumptions that the excitation satisfies the equal energy and non-correlation condition (41) and the reflection symmetry $\Xi(p, q) = \Xi(-p, q)$. This factorization property can be verified after obtaining the dispersion relations by confirming that the perturbations to the covariance matrix associated with VSHFI produce no eddy buoyancy flux divergences, and vice versa for those associated with HMBLI.

The VSHFI dispersion relation is obtained by setting $\hat{B} = 0$ in (C16)-(C21) so that the horizontal mean structure corresponds to a VSHF with no mean buoyancy perturbation. Equations (C16)-(C19) can then be solved for $\tilde{\Psi}$ to obtain

$$\tilde{\Psi} = ips' \hat{U} \frac{(\tilde{\Phi}_H^+ - \tilde{\Phi}_H^-) F_0 + (\tilde{T}_H^+ - \tilde{T}_H^-) (2p^2 h_-^2 h_+^2)}{F_0^2 - 4p^4 N_0^4 h_-^2 h_+^2}, \quad (\text{C22})$$

where $F_0 = s'^2 h_-^2 h_+^2 + 2p^2 N_0^2 (h^2 + \frac{m^2}{4})$ and $h_\pm^2 = p^2 + (q \pm \frac{1}{2}m)^2$. The assumption that $\hat{B} = 0$ can be shown to be consistent by similarly solving (C16)-(C19) for \tilde{S}^{diff} (not shown) and substituting the result into (C21). Inspection of the right-hand side of the resulting equation reveals that the integral representing the eddy buoyancy flux divergence vanishes by symmetry if the excitation is reflection symmetric.

Substituting (C22) into (C20) and simplifying we obtain the expression

$$\bar{s}_U = \varepsilon \iint dp dq s_U'' \mathcal{F}_U(p, q, m, N_0^2, r, v, s_U) \tilde{E}(p, q), \quad (\text{C23})$$

in which we have defined $s_{U,B}'' = s_{U,B} + 2(r + v(h^2 + m(q + m/2)))$. The feedback factor \mathcal{F}_U is given by

$$\mathcal{F}_U = \frac{mp^2 h^2 (q + \frac{m}{2})}{(r + v h^2)(2\pi)^2} \times \frac{(1 - \frac{m^2}{h^2})[s_U'' h^2 h_{++}^2 + 2p^2 N_0^2 (h^2 + m(q + \frac{m}{2}))] + 2p^2 h_{++}^2 N_0^2}{[s_U'' h^2 h_{++}^2 + 2p^2 N_0^2 (h^2 + m(q + \frac{m}{2}))]^2 - 4p^4 N_0^4 h^2 h_{++}^2},$$

where $h_{++}^2 = p^2 + (q + m)^2$. If $v = 0$ the factor s_U'' in (C23) may be brought to the left-hand side and we obtain the dispersion relation in the form (47).

To obtain the HMBLI dispersion relation we proceed similarly, setting $\hat{U} = 0$ in (C16)-(C21) so that the horizontal mean structure corresponds to an HMBL with no mean flow perturbation. Solving equations (C16)-(C19) for \tilde{S}^{diff} , substituting into (C21), and simplifying, we obtain

$$\bar{s}_B = \varepsilon \int dp dq s_B'' \mathcal{F}_B(p, q, m, N_0^2, r, v, s_B) \tilde{E}(p, q). \quad (\text{C25})$$

The feedback factor \mathcal{F}_B is given by

$$\mathcal{F}_B = \frac{h^2 m^2 p^2 h_{++}^4}{2(r + v h^2)(2\pi)^2} \frac{s_B'' h^2 h_{++}^2 + 2p^2 m(q + m/2) N_0^2}{m^2 (q + m/2)^2 F_1^2 - F_2 F_3}, \quad (\text{C26})$$

in which the functions $F_{1,2,3}$ are given by

$$F_1 = h^2 h_{++}^2 s_B''^2 + 2p^2 N_0^2 (h^2 + m(q + m/2)), \quad (\text{C27})$$

$$F_2 = h^2 h_{++}^2 (h^2 + m(q + m/2)) s_B''^2 + 2m^2 p^2 (q + m/2)^2 N_0^2, \quad (\text{C28})$$

$$F_3 = h^2 h_{++}^2 (h^2 + m(q + \frac{m}{2})) s_B''^2 + 2p^2 N_0^2 ((h^2 + m(q + \frac{m}{2}))^2 + h^2 h_{++}^2). \quad (\text{C29})$$

As in the case of VSHFI, the assumption that $\hat{U} = 0$ can be shown to be consistent by solving (C16)-(C19) for $\tilde{\Psi}$, substituting the result into (C20), and verifying that the integral on the right-hand side of the resulting equation, which represents the eddy momentum flux divergence, vanishes by symmetry for excitation satisfying reflection symmetry.

APPENDIX D

Analysis of VSHFI in the case of Isotropic Ring Excitation (IRE)

(i) Mathematical formulation of IRE

(C24) Isotropic ring excitation is defined by the excitation spectra

$$\tilde{\Xi}(p, q) = 2\pi k_e \delta(h - k_f), \quad \tilde{\Theta}(p, q) = 2\pi N_0^2 k_e^{-1} \delta(h - k_f), \quad (\text{D1})$$

with $\tilde{G}^\zeta = \tilde{G}^b = 0$. The excitation (D1) satisfies the equal-energy and non-correlation conditions (41). In physical space, the excitation covariances are given by

$$\Xi(x, z) = k_e^2 J_0(k_e r), \quad \Theta(x, z) = N_0^2 J_0(k_e r), \quad (\text{D2})$$

where $r = \sqrt{x^2 + z^2}$ and J_0 is the zeroth-order Bessel function of the first kind. Hereafter we work in nondimensional units in which the unit of length is set by the excitation scale, $1/k_e$, and the unit of time is set by the perturbation damping time, $1/r$. In these units the energy excitation spectrum for IRE is given by (49).

(ii) Dispersion relation and feedback factor

To obtain explicit expressions for the dispersion relation and feedback factor for VSHFI we evaluate equations (C23) and (C24) with the excitation spectrum (49). We obtain

$$\bar{s}_U = \varepsilon \int_0^{2\pi} d\theta (2\pi s_U'') \left\{ \frac{m \cos^2 \theta (\sin \theta + m/2)}{(2\pi)^2 (1 + v)} \times \frac{s_U'' (1 - m^2) (1 + 2m \sin \theta + m^2) + N_0^2 \cos^2 \theta [4 + m^2 (1 - m^2) - 2m(m^2 - 3) \sin \theta]}{[s_U'' (1 + 2m \sin \theta + m^2) + \cos^2 \theta N_0^2 (2 + 2m \sin \theta + m^2)]^2 - 4 \cos^4 \theta N_0^4 (1 + 2m \sin \theta + m^2)} \right\}. \quad (\text{D3})$$

In this equation the explicit nondimensional forms of \bar{s}_U and s_U'' for IRE are given by $\bar{s}_U = s_U + r_m + v m^2$ and

$s_U'' = s_U + 2(1 + v(1 + m(\sin \theta + m/2)))$. The factor in braces in (D3) gives the explicit form of the feedback factor, \mathcal{F}_U , that is relevant to the case of IRE as discussed in Section 7. Note that the factor of 2π outside the braces originates from (49) and so is not included in \mathcal{F}_U . Explicit formulae for the HMBLI dispersion relation and feedback factor can be obtained by a similar procedure in which equations (C25) and (C26) are evaluated using the excitation spectrum (49).

(iii) Asymptotic analysis

We now provide details on the derivation of various asymptotic approximations useful for understanding the properties of VSHFI in the case of IRE. For simplicity we set $v = 0$ throughout.

To obtain the estimate (50) for the VSHF growth rate under weak stratification, we first note that in the case $N_0^2 = 0$ the dispersion relation (D3) simplifies to

$$\bar{s}_U s_U' = \varepsilon m(1 - m^2) \int_0^{2\pi} \frac{d\theta \cos^2 \theta (\sin \theta + m/2)}{2\pi (1 + 2m \sin \theta + m^2)}. \quad (\text{D4})$$

The integral on the right-hand side of (D4) is equal to zero for $0 < m < 1$, and the VSHF growth rate is then given by $s_U = -r_m$. To obtain the leading order correction to this $N_0^2 = 0$ solution we substitute the expansion $s_U = -r_m + s_1 N_0^2 + \mathcal{O}(N_0^4)$ into (D3) and expand the integrand in a power series in N_0^2 , retaining terms up to order N_0^2 . This procedure gives a number of integrals similar in form to the integral in (D4), all of which can be evaluated in closed form. Solving the resulting expression for s_1 gives the result (50).

To obtain the expressions (51)-(52), which illustrate that VSHFI is associated with negative eddy viscosity, we

analyze the dispersion relation (D3) in the limit of very large-scale VSHFs, corresponding to small m . For $m = 0$ the VSHF growth rate is given by the explicit damping rate, $s_U = -r_m$, which can be verified by inspection of (D3). For small m we write the VSHFI growth rate as $s_U = -r_m + s_1 m^2 + \mathcal{O}(m^4)$, omitting terms of odd order as s_U does not depend on the sign of m . Substituting this expression into (D3) and retaining terms in the expansion up to order m^2 gives a sum of integrals that can be evaluated in closed form. Solving the resulting expression for s_1 gives

$$s_1 = \varepsilon g(N_0^2, r_m), \quad (\text{D5})$$

where g is defined by

$$g(N_0^2, r_m) = \frac{1}{16s_0'} \left\{ 1 - \frac{s_0'^2}{N_0^2} (1 - 2f) - \frac{s_0'^4}{2N_0^4} (1 - f) \right\}, \quad (\text{D6})$$

in which we have used the notation $s_0' = 2 - r_m$ and defined the function $f(r_m, N_0^2) = s_0' (4N_0^2 + s_0'^2)^{-1/2}$. Equation (51) identifies the eddy viscosity, v_{eddy} , with the negative of the growth rate correction, $-s_1$, which gives the result (52). Analysis of $g(N_0^2, r_m)$ reveals that $g > 0$ for all N_0^2 , so that the eddy viscosity is negative.

To obtain the estimate (53) of the VSHF growth rate in the case of strong stratification we analyze the dispersion relation (D3) in the limit of large N_0^2 . As $N_0^2 \rightarrow \infty$, inspection of (D3) shows that $s_U \rightarrow -r_m$. To obtain the leading-order correction for large but finite N_0^2 , we write the dispersion relation terms of the small parameter $\delta \equiv 1/N_0^2$ as

$$\bar{s}_U = m\varepsilon\delta s_0' \int \frac{d\theta}{2\pi} I(\delta, \theta), \quad (\text{D7})$$

where the integrand is given by

$$I = \frac{\cos^4 \theta (\sin \theta + m/2) [4 + m^2 (1 - m^2) - 2m(m^2 - 3) \sin \theta] + \mathcal{O}(\delta)}{m^2 \cos^4 \theta (2 \sin \theta + m)^2 + \delta [2s_0'^2 \cos^2 \theta (1 + 2m \sin \theta + m^2) (2 + 2m \sin \theta + m^2)] + \mathcal{O}(\delta^2)}. \quad (\text{D8})$$

The factor of δ outside the integral in (D7) indicates that the correction to the growth rate decays at least as fast as $1/N_0^2$. To obtain the explicit form of the correction, we evaluate the integral using the residue theorem. The integral of $I(\delta, \theta)$ is undefined for $\delta = 0$ due to the presence of poles at the solutions of $2 \sin \theta + m = 0$ which exist when $0 < m < 2$. These poles are shifted into the complex plane for small but nonzero δ by the $\mathcal{O}(\delta)$ term in the denominator. To apply the residue theorem we use a rectangular contour in the complex plane that includes the real interval $[0, 2\pi]$ and is closed in the upper half plane. To use this contour we must ensure that the integrand, $I(\delta, \theta)$, vanishes as $\theta \rightarrow +i\infty$. However, I does not vanish in this

limit and instead converges to

$$\lim_{\theta \rightarrow +i\infty} I(\delta, \theta) = \frac{3 - m^2}{2m}, \quad (\text{D9})$$

and so the residue theorem cannot be applied directly to (D7). This issue is resolved by adding and subtracting this limiting value inside the integral in (D7) to obtain

$$\bar{s}_U = m\varepsilon\delta s_0' \int \frac{d\theta}{2\pi} \left[I(\delta, \theta) - \frac{3 - m^2}{2m} \right] + \frac{1}{2} \varepsilon \delta s_0' (3 - m^2). \quad (\text{D10})$$

The integral in (D10) can be evaluated using the residue theorem. Due to the 2π -periodicity of the integrand, the

vertical branches of the contour integral cancel one another, and detailed calculation of the residues shows that the contributions from the poles also sum to zero so that the integral in (D10) equals zero at the lowest order in δ . The growth rate estimate (53) is then obtained by solving (D10) for s_U .

To obtain asymptotic estimates for the stability boundary, $\varepsilon_c(m)$, in the limits of weak and strong stratification, we follow identical procedures for expanding and evaluating the integral in (55) as were used to obtain the asymptotic growth rate estimates in those limits, except that we set $s_U = 0$ rather than expanding about $s_U = -r_m$. In the limit of weak stratification we obtain

$$\varepsilon_c(m) \approx \frac{64r_m}{m^2 N_0^2}, \quad (\text{D11})$$

which is valid for $m < 1$. The first VSHF wavenumber to become unstable is then $m^* = 1$, and so the stability boundary is given by $\varepsilon_c \approx 64r_m/N_0^2$. In the limit of strong stratification we obtain

$$\varepsilon_c(m) \approx \frac{r_m N_0^2}{3 - m^2} \quad (\text{D12})$$

which is valid for $m < \sqrt{3}$, as ε must be positive. In this case the first VSHF wavenumber to become unstable tends

to $m^* = 0$ as $N_0^2 \rightarrow \infty$, and so the stability boundary is given by $\varepsilon_c \approx r_m N_0^2/3$. These estimates are shown in Figure 7 (a).

APPENDIX E

Analysis of VSHFI in the case of Monochromatic Excitation (MCE)

(i) Dispersion relation

MCE is defined by the energy injection spectrum (54), which corresponds to the vorticity and buoyancy excitation spectra

$$\tilde{\Xi} = \pi^{3/2} \ell_c (1 + q^2) \exp(-\ell_c^2 q^2/4) [\delta(p+1) + \delta(p-1)] \quad (\text{E1})$$

$$\tilde{\Theta} = N_0^2 \pi^{3/2} \ell_c \exp(-\ell_c^2 q^2/4) [\delta(p+1) + \delta(p-1)] \quad (\text{E2})$$

As in the case of IRE, we obtain the VSHFI dispersion relation in the case of MCE by evaluating (C23) and (C24) with the excitation spectrum (54). We obtain

$$\bar{s}_U = \varepsilon \int_{-\infty}^{\infty} dq s''_U \left(2\pi^{3/2} \ell_c e^{-\ell_c^2 q^2/4} \right) \left\{ \frac{m(q+m/2)(1+q^2)}{(2\pi)^2(1+v(1+q^2))} \times \right. \\ \left. \frac{\left(1 - \frac{m^2}{1+q^2}\right) [s''_U(1+q^2)(1+(q+m)^2) + 2N_0^2(1+q^2+m(q+m/2))] + 2N_0^2(1+(q+m)^2)}{[s''_U(1+q^2)(1+(q+m)^2) + 2N_0^2(1+q^2+m(q+m/2))]^2 - 4N_0^4(1+q^2)(1+(q+m)^2)} \right\}, \quad (\text{E3})$$

in which $\bar{s}_U = s_U + r_m + v m^2$ and $s''_U = s_U + 2(1 + v(1 + q^2 + m(q+m/2)))$. The factor in braces in (E3) gives the explicit form of the feedback factor, \mathcal{F}_U , that is relevant to the case of MCE. Explicit formulae for the HMBLI dispersion relation and feedback factor in the case of MCE can be obtained by evaluating (C25) and (C26) using the excitation spectrum (54).

(ii) Asymptotic analysis

To obtain a closed form estimate of the VSHFI growth rate in the case of MCE under strong stratification, we expand (E3) in the small parameter $\delta = 1/N_0^2$ to obtain

$$\bar{s}_U = \delta \frac{\varepsilon \ell_c s'_0}{2m\sqrt{\pi}} \int_{-\infty}^{\infty} dq e^{-\ell_c^2 q^2/4} \frac{J(q)}{(m+2q) + \mathcal{O}(\delta)}. \quad (\text{E4})$$

where we have set $v = 0$ for simplicity and defined $s'_0 = 2 - r_m$ and $J(q) = (1 + (q+m)^2)(1+q^2) + (1+q^2+m(q+m/2))$.

As in the case of IRE, the factor of δ outside the integral indicates that \bar{s}_U decays at least as fast as $1/N_0^2$ as the stratification is increased. The integral in (E4) is undefined for $\delta = 0$ due to the pole at $q = -m/2$. However, the value of the integral converges to a well-defined limit as $\delta \rightarrow 0$, which can be evaluated as follows. To regularize the $\delta = 0$ integral at $q = -m/2$, we rewrite (E4) as

$$\bar{s}_U = \delta \frac{\varepsilon \ell_c s'_0}{2m\sqrt{\pi}} \left\{ \int_{-\infty}^{\infty} dq e^{-\ell_c^2 q^2/4} \frac{J(q) - J(-m/2)}{(m+2q) + \mathcal{O}(\delta)} \right. \\ \left. + J(-m/2) \int_{-\infty}^{\infty} dq \frac{e^{-\ell_c^2 q^2/4}}{(m+2q) + \mathcal{O}(\delta)} \right\} \quad (\text{E5})$$

The first integral in (E5) is no longer singular at $q = -m/2$ for $\delta = 0$ and can be evaluated in closed form. The second integral remains singular at $\delta = 0$. However, it can be

assigned a finite Cauchy principal value as $\delta \rightarrow 0$, and in fact can be recognized, after minor manipulations, as the Hilbert transform of a Gaussian function. We then obtain

$$s_U \approx -r_m + (1 - r_m/2) \frac{\ell_c \varepsilon}{N_0^2} S(m), \quad (\text{E6})$$

where the function S is given by

$$S(m) = \frac{4 + \ell_c^2}{\ell_c^3} - \frac{3}{4\ell_c} m^2 + \left(\frac{2}{m} - \frac{m^3}{8} \right) F\left(\frac{\ell_c m}{4}\right), \quad (\text{E7})$$

in which F is the Dawson function. This approximation is shown in Figure 6.

An asymptotic estimate for the stability boundary, ε_c , can be obtained by applying similar methods to approximate the integral in (55). In the limit of strong stratification we obtain

$$\varepsilon_c(m) \approx \frac{r_m N_0^2}{\ell_c S(m)}. \quad (\text{E8})$$

In this limit the minimum of $\varepsilon_c(m)$ occurs at $m^* = 0$, so that the stability boundary is given by

$$\varepsilon_c \approx \frac{2r_m \ell_c^2}{\ell_c^4 + 2\ell_c^2 + 8} N_0^2. \quad (\text{E9})$$

This estimate is shown in Figure 7 (a).

APPENDIX F

Decomposition of the Feedback Factor into Contributions from Individual Processes

In this Appendix we provide mathematical details relevant to Section 8 in which the VSHFI feedback factor, \mathcal{F}_U , for which the general expression is given by (C24), is decomposed into the feedback contributions from individual processes. For simplicity we set $\nu = 0$.

When solving (C16)–(C19) for $\tilde{\Psi}$, as described in Appendix C, the solution can be decomposed as

$$\tilde{\Psi} = \tilde{\Psi}^{Orr} + \tilde{\Psi}^{cu} + \tilde{\Psi}^{wave}, \quad (\text{F1})$$

where the individual contributions are defined by the term in (43) from which they each originate, as described in Section 8. The contributions are given by

$$\tilde{\Psi}^{Orr} = -ip\hat{U} \frac{h_-^4 \tilde{\Psi}_H^- - h_+^4 \tilde{\Psi}_H^+}{s'_U h_-^2 h_+^2}, \quad (\text{F2})$$

$$\tilde{\Psi}^{cu} = im^2 p\hat{U} \frac{h_-^2 \tilde{\Psi}_H^- - h_+^2 \tilde{\Psi}_H^+}{s'_U h_-^2 h_+^2}. \quad (\text{F3})$$

The contribution from wave dynamics, $\tilde{\Psi}^{wave}$, can be obtained most simply as a residual using (F1) and (C22). Combining the decomposition (F1) with equations (C20) and (C23) yields the decomposition (58).

References

- Ascani, F., E. Firing, J. P. McCreary, P. Brandt, and R. J. Greatbatch, 2015: The deep equatorial ocean circulation in wind-forced numerical solutions*. *J. Phys. Oceanogr.*, **45**, 1709–1734.
- Bakas, N. A., N. C. Constantinou, and P. J. Ioannou, 2015: S3T stability of the homogeneous state of barotropic beta-plane turbulence. *J. Atmos. Sci.*, **72** (5), 1689–1712.
- Bakas, N. A., N. C. Constantinou, and P. J. Ioannou, 2017: Statistical state dynamics of weak jets in barotropic beta-plane turbulence. *arXiv.org*, 1708.03031v1.
- Bakas, N. A., and P. J. Ioannou, 2011: Structural stability theory of two-dimensional fluid flow under stochastic forcing. *J. Fluid Mech.*, **682**, 332–361.
- Bakas, N. A., and P. J. Ioannou, 2013a: Emergence of large scale structure in barotropic beta-plane turbulence. *Phys. Rev. Lett.*, **110** (22).
- Bakas, N. A., and P. J. Ioannou, 2013b: On the mechanism underlying the spontaneous emergence of barotropic zonal jets. *J. Atmos. Sci.*, **70** (7), 2251–2271.
- Bakas, N. A., and P. J. Ioannou, 2014: A theory for the emergence of coherent structures in beta-plane turbulence. *J. Fluid Mech.*, **740**, 312–341.
- Baldwin, M. P., and Coauthors, 2001: The quasi-biennial oscillation. *Rev. Geophys.*, **39**, 179–229.
- Bernstein, J., and B. F. Farrell, 2010: Low-frequency variability in a turbulent baroclinic jet: Eddy-mean flow interactions in a two-level model. *J. Atmos. Sci.*, **67** (2), 452–467.
- Brethouwer, G., P. Billant, E. Lindborg, and J. M. Chomaz, 2007: Scaling analysis and simulation of strongly stratified turbulent flows. *J. Fluid Mech.*, **585**, 343–368.
- Constantinou, N. C., B. F. Farrell, and P. J. Ioannou, 2014: Emergence and equilibration of jets in beta-plane turbulence: Applications of stochastic structural stability theory. *J. Atmos. Sci.*, **71** (5), 1818–1842.
- Constantinou, N. C., B. F. Farrell, and P. J. Ioannou, 2016: Statistical state dynamics of jet-wave coexistence in barotropic beta-plane turbulence. *J. Atmos. Sci.*, **73** (5), 2229–2253.
- Farrell, B. F., and P. J. Ioannou, 2003: Structural stability of turbulent jets. *J. Atmos. Sci.*, **60** (17), 2101–2118.
- Farrell, B. F., and P. J. Ioannou, 2007: Structure and spacing of jets in barotropic turbulence. *J. Atmos. Sci.*, **64** (10), 3652–3665.
- Farrell, B. F., and P. J. Ioannou, 2008: Formation of jets by baroclinic turbulence. *J. Atmos. Sci.*, **65** (11), 3353–3375.
- Farrell, B. F., and P. J. Ioannou, 2009: A stochastic structural stability theory model of the drift wave-zonal flow system. *Phys. Plasmas*, **16**, 112 903.
- Farrell, B. F., and P. J. Ioannou, 2009a: Emergence of jets from turbulence in the shallow-water equations on an equatorial beta plane. *J. Atmos. Sci.*, **66** (10), 3197–3207.
- Farrell, B. F., and P. J. Ioannou, 2009b: A theory of baroclinic turbulence. *J. Atmos. Sci.*, **66** (8), 2444–2454.

- Farrell, B. F., and P. J. Ioannou, 2017a: Statistical state dynamics: A new perspective on turbulence in shear flow. *Zonal Jets: Phenomenology, Genesis, Physics*, B. Galperin, and P. L. Read, Eds., Cambridge University Press.
- Farrell, B. F., and P. J. Ioannou, 2017b: Statistical state dynamics based theory for the formation and equilibration of Saturn's North polar jet. *Phys. Rev. Fluids*, **2** (7).
- Fitzgerald, J. G., and B. F. Farrell, 2016: Statistical state dynamics of vertically sheared horizontal flows in two-dimensional stratified turbulence. *arXiv.org*, 1612.03243v2.
- Galperin, B., and P. L. Read, Eds., 2017: *Zonal Jets: Phenomenology, Genesis, Physics*. Cambridge University Press.
- Galperin, B., S. Sukoriansky, N. Dikovskaya, P. L. Read, Y. H. Yamazaki, and R. Wordsworth, 2006: Anisotropic turbulence and zonal jets in rotating flows with a beta-effect. *Nonlinear Process. Geophys.*, **13** (1), 83–98.
- Herbert, C., R. Marino, D. Rosenberg, and A. Pouquet, 2016: Waves and vortices in the inverse cascade regime of stratified turbulence with or without rotation. *J. Fluid Mech.*, **806**, 165–204.
- Herring, J. R., 1963: Investigation of problems in thermal convection. *J. Atmos. Sci.*, **20**, 325–338.
- Holton, J. R., and R. S. Lindzen, 1972: An updated theory for the quasi-biennial cycle of the tropical stratosphere. *J. Atmos. Sci.*, **29** (6), 1076–1080.
- Hua, B. L., M. D'orgeville, and M. D. Fruman, 2008: Destabilization of mixed Rossby gravity waves and the formation of equatorial zonal jets. *J. Fluid Mech.*, **610**, 311–341.
- Huang, H.-P., and W. A. Robinson, 1998: Two-dimensional turbulence and persistent zonal jets in a global barotropic model. *J. Atmos. Sci.*, **55** (4), 611–632.
- Kumar, A., M. K. Verma, and J. Sukhatme, 2017: Phenomenology of two-dimensional stably stratified turbulence under large-scale forcing. *J. Turbul.*, **18** (3), 219–239.
- Laval, J. P., J. McWilliams, and B. Dubrulle, 2003: Forced stratified turbulence: Successive transitions with Reynolds number. *Phys. Rev. E*, **68** (3), 036308.
- Marino, R., P. D. Mininni, D. L. Rosenberg, and A. Pouquet, 2014: Large-scale anisotropy in stably stratified rotating flows. *Phys. Rev. E*, **90** (2), 023018.
- Marston, J. B., 2010: Statistics of the general circulation from cumulant expansions. *Chaos*, **20** (4).
- Marston, J. B., 2012: Planetary atmospheres as nonequilibrium condensed matter. *Annu. Rev. Condens. Matter Phys.*, **3**, 285–310.
- Maximenko, N. A., B. Bang, and H. Sasaki, 2005: Observational evidence of alternating zonal jets in the world ocean. *Geophys. Res. Lett.*, **32** (12).
- McCreary, J. P., 1984: Equatorial beams. *J. Mar. Res.*, **42**, 395–430.
- Muench, J. E., and E. Kunze, 1999: Internal wave interactions with equatorial deep jets. Part I: Momentum-flux divergences. *J. Phys. Oceanogr.*, **29** (7), 1453–1467.
- Parker, J. B., and J. A. Krommes, 2013: Zonal flow as pattern formation. *Phys. Plasmas*, **20** (10).
- Parker, J. B., and J. A. Krommes, 2014: Generation of zonal flows through symmetry breaking of statistical homogeneity. *New J. Phys.*, **16**, 035006.
- Plumb, R. A., 1977: The interaction of two internal waves with the mean flow: Implications for the theory of the quasi-biennial oscillation. *J. Atmos. Sci.*, **34**, 1847–1858.
- Plumb, R. A., and A. D. McEwan, 1978: The instability of a forced standing wave in a viscous stratified fluid: A laboratory analogue of the quasi-biennial oscillation. *J. Atmos. Sci.*, **35**, 1827–1839.
- Read, P. L., Y. H. Yamazaki, S. R. Lewis, P. D. Williams, R. Wordsworth, K. Miki-Yamazaki, J. Sommeria, and H. Didelle, 2007: Dynamics of convectively driven banded jets in the laboratory. *J. Atmos. Sci.*, **64** (11), 4031–4052.
- Rhines, P. B., 1975: Waves and turbulence on a beta-plane. *J. Fluid Mech.*, **69**, 417–443.
- Rorai, C., P. D. Mininni, and A. Pouquet, 2015: Stably stratified turbulence in the presence of large-scale forcing. *Phys. Rev. E*, **92** (1), 013003.
- Salmon, R., 1982: Geostrophic turbulence. *Topics in Ocean Physics*, A. R. Osborne, and P. M. Rizzoli, Eds., Italian Physical Society, Bologna, Italy.
- Smith, L. M., 2001: Numerical study of two-dimensional stratified turbulence. *Advances in Wave Interaction and Turbulence*, P. A. Milewski, L. M. Smith, F. Waleffe, and E. G. Tabak, Eds., Amer. Math Soc., Providence, RI.
- Smith, L. M., and F. Waleffe, 2002: Generation of slow large scales in forced rotating stratified turbulence. *J. Fluid Mech.*, **451**, 145–168.
- Squire, J., and A. Bhattacharjee, 2015: Statistical simulation of the magnetorotational dynamo. *Phys. Rev. Lett.*, **114** (8), 085002.
- Srinivasan, K., and W. R. Young, 2012: Zonostrophic instability. *J. Atmos. Sci.*, **69** (5), 1633–1656.
- St-Onge, D. A., and J. A. Krommes, 2017: Zonostrophic instability driven by discrete particle noise. *Phys. Plasmas*, **24** (4).
- Taylor, J. R., 2008: Numerical simulations of the stratified oceanic bottom boundary layer. Ph.D. thesis, University of California, San Diego.
- Tobias, S. M., K. Dagon, and J. B. Marston, 2011: Astrophysical fluid dynamics via direct statistical simulation. *Astrophys. J.*, **727**, 127.
- Tobias, S. M., and J. B. Marston, 2013: Direct statistical simulation of out-of-equilibrium jets. *Phys. Rev. Lett.*, **110** (10), 104502.
- Vasavada, A. R., and A. P. Showman, 2005: Jovian atmospheric dynamics: An update after Galileo and Cassini. *Rep. Prog. Phys.*, **68** (8), 1935–1996.
- Waite, M. L., and P. Bartello, 2004: Stratified turbulence dominated by vortical motion. *J. Fluid Mech.*, **517**, 281–308.
- Waite, M. L., and P. Bartello, 2006: Stratified turbulence generated by internal gravity waves. *J. Fluid Mech.*, **546**, 313–339.
- Williams, G. P., 1978: Planetary circulations: 1. Barotropic representation of Jovian and terrestrial turbulence. *J. Atmos. Sci.*, **35** (8), 1399–1426.

- Wunsch, C., 1977: Response of an equatorial ocean to a periodic monsoon. *J. Phys. Oceanogr.*, **7** (4), 497–511. 2134–2148.
- Youngs, M. K., and G. C. Johnson, 2015: Basin-wavelength equatorial deep jet signals across three oceans*. *J. Phys. Oceanogr.*, **45** (8),